PNAS RESEARCH ARTICLE | PHYSICS

Real-space imaging of periodic nanotextures in thin films via phasing of diffraction data

Ziming Shao[a], Noah Schnitzer[a], Jacob Ruf[b], Oleg Yu. Gorobtsov[a], Cheng Dai[c], Berit H. Goodge[d,e], Tiannan Yang[c], Hari Nair[a], Vlad A. Stoica[c,f], John W. Freeland[f], Jacob P. Ruff[g], Long-Qing Chen[c], Darrell G. Schlom[a,e,h], Kyle M. Shen[b,e], Lena F. Kourkoutis[d,e], and Andrej Singer[a,1]

Edited by Angel Rubio, Max-Planck-Institut fur Struktur und Dynamik der Materie, Hamburg, Germany; received February 27, 2023; accepted May 11, 2023

New properties and exotic quantum phenomena can form due to periodic nanotextures, including Moire patterns, ferroic domains, and topologically protected magnetization and polarization textures. Despite the availability of powerful tools to characterize the atomic crystal structure, the visualization of nanoscale strain-modulated structural motifs remains challenging. Here, we develop nondestructive real-space imaging of periodic lattice distortions in thin epitaxial films and report an emergent periodic nanotexture in a Mott insulator. Specifically, we combine iterative phase retrieval with unsupervised machine learning to invert the diffuse scattering pattern from conventional X-ray reciprocal-space maps into real-space images of crystalline displacements. Our imaging in $PbTiO_3/SrTiO_3$ superlattices exhibiting checkerboard strain modulation substantiates published phase-field model calculations. Furthermore, the imaging of biaxially strained Mott insulator Ca_2RuO_4 reveals a strain-induced nanotexture comprised of nanometer-thin metallic-structure wires separated by nanometer-thin Mott-insulating-structure walls, as confirmed by cryogenic scanning transmission electron microscopy (cryo-STEM). The nanotexture in Ca_2RuO_4 film is induced by the metal-to-insulator transition and has not been reported in bulk crystals. We expect the phasing of diffuse X-ray scattering from thin crystalline films in combination with cryo-STEM to open a powerful avenue for discovering, visualizing, and quantifying the periodic strain-modulated structures in quantum materials.

epitaxial thin film | mott insulator | X-ray imaging | coherent diffractive imaging

Significance

Coherent X-ray diffractive imaging (CXDI) has been widely applied to study the strain distribution in confined systems using an illuminating beam with high spatial coherence. Here, we broaden the capability of CXDI by imaging the strained structural motifs in periodic nanotextured epitaxial thin films with unprecedented nanoscale resolution, exploiting the diffuse scattering pattern from a conventional, partially coherent synchrotron beam. We demonstrate the technique by discovering a previously unreported nanotexture in a Mott insulator epitaxial thin film, which is confirmed by cryo-STEM. The work promises to become a stepping stone for quantifying periodic strain-modulated structures in ferroics and topological quantum materials.

Strain engineering in the epitaxial thin films exploits uniform biaxial strain imposed by substrate clamping for manipulating the electronic, magnetic, or structural properties of quantum materials and microelectronics (1). Yet, spontaneously forming magnetic and electronic nanotextures (2–4) or artificially engineered Moire structures (5) revealed by scanning probe techniques (6–10) challenge the existing sophisticated X-ray characterization tools, such as JANA2006 (11), COBRA (12), and protein crystallography (13), to perform the structural determination of nonuniform strain modulations. A possible solution for quantitative determination of static nonuniform strain modulations leverages the X-ray diffuse scattering patterns, opening prospects for dynamical studies in the future.

In the kinematical approximation, the diffracted X-ray intensities, $I\left(\vec{Q}\right)$, relate to the density of scatterers, $\rho\left(\vec{r}\right)$, through a Fourier transform $I\left(\vec{Q}\right) = A\left|\int \rho\left(\vec{r}\right)\exp\left(-i\vec{Q}\cdot\vec{r}\right)d\vec{r}\right|^2$, where $\vec{Q}$ is the momentum transfer in reciprocal space, $\vec{r}$ is the real-space coordinate, and A is a constant. In structures with a periodically modulated $\rho\left(\vec{r}\right)$, X-ray interference generates intensity maxima, whose positions, relative intensities, and shapes allow studying the structure of the crystal unit cell, crystal lattice (14), and mesoscale strain modulations (15). The Fourier transform is invertible, yet the notorious phase problem—one can only measure X-ray photon intensities, not their phases—prevents a direct inversion of the X-ray data into a real-space structure. As proposed by Sayre (16, 17), diffraction data can be inverted if intensities between Bragg reflections are recorded. Sayre's idea culminated in the development of coherent X-ray diffractive imaging (CXDI) (18–24): a lensless imaging technique with the resolution, in principle, limited only by the wavelength and the strength of the scattering signal. Akin to laser diffraction on a pinhole, a coherent X-ray beam scattered off a spatially confined specimen produces interference fringes. These fringes can be inverted into a real-space image if the entire specimen is illuminated with a spatially coherent X-ray beam and the specimen size is small enough for the interference fringes (spaced inversely proportional to the specimen size) to be measured with sufficient resolution (25, 26). CXDI has been used for visualizing biological cells (27, 28), strain in nanocrystals (20, 29), and recently

Author contributions: D.G.S., K.M.S., L.F.K., and A.S. designed research; Z.S., N.S., J.R., B.H.G., H.N., V.A.S., J.W.F., and J.P.R. performed research; Z.S., J.R., O.Y.G., C.D., T.Y., H.N., L.-Q.C., and A.S. contributed new reagents/analytic tools; Z.S. and N.S. analyzed data; and Z.S., N.S., L.F.K., and A.S. wrote the paper.

The authors declare no competing interest.

This article is a PNAS Direct Submission.

[1]To whom correspondence may be addressed. Email: asinger@cornell.edu.

This article contains supporting information online at https://www.pnas.org/lookup/suppl/doi:10.1073/pnas.2303312120/-/DCSupplemental.

Published July 6, 2023.

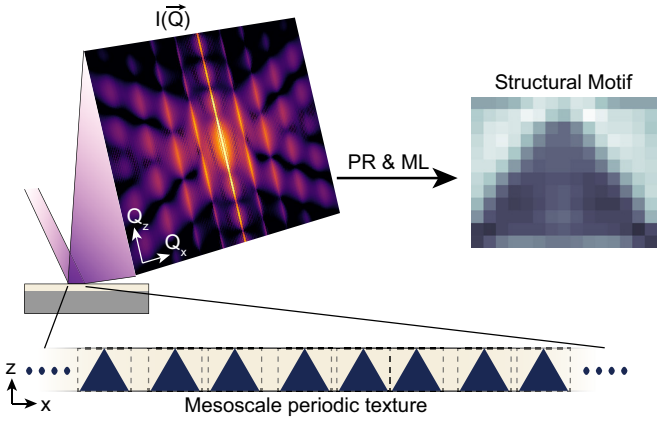

Fig. 1. Real-space imaging of nanotextures in crystalline thin films. In a reciprocal space map (RSM), the mesoscale periodic ordering is evident from satellite peaks around the Bragg reflection. The diffraction intensity, $I(\vec{Q})$, shown here is an average of the squared magnitudes of Fourier transforms of schematic periodic textures with triangular motifs, where the dark area has a constant strain difference compared to the surrounding light area. The motifs are placed with stochastic intervals in the texture exhibiting a translational ordering along the x-axis. The structural motif is retrieved by phasing the diffraction data through a combination of phase retrieval (PR) and unsupervised machine learning (ML). The code required for generating results shown is available here: https://github.com/ZimingS/Periodic-Textures-Imaging.

operando changes in energy materials (30, 31) and single macromolecules at free-electron lasers (32, 33).

Interference fringes can also emerge around a Bragg reflection of single-crystalline thin films as "satellite peaks" or diffuse X-ray scattering when a periodic strain modulation is present (2, 4, 34, 35). These satellite peaks occur even when measured on large samples with an X-ray beam of poor spatial coherence. Consider an arrangement of structural motifs, which displays short-range periodicity over small areas (see Fig. 1). Despite the lack of long-range periodicity and the missing confinement in the horizontal direction (x in Fig. 1), the diffracted intensity of such a structure displays well-defined satellite peaks in addition to the sharp central Bragg peak and Laue fringes due to confinement in the vertical direction (z in Fig. 1). The satellite peaks persist even with slight distortions in the short-range order (note the differing distances between the triangles from spot to spot in Fig. 1). Apart from a few exceptions, a strategy to analyze the X-ray data entails refining a model by comparing its calculated diffraction intensity with the measured one (34). Constructing a model often requires sophisticated phase-field modeling (4). Often, only qualitative agreement can be achieved between the model and experimentally measured diffraction pattern, suggesting that the refined models may remain incomplete. Here, we develop a model-independent approach by combining conventional iterative phase retrieval (36) with unsupervised machine learning (37, 38) to extract high-resolution images of the structural motifs from the diffraction intensities measured from epitaxial thin crystalline films (such as the one shown in Fig. 1). The method is akin to crystallography: We reveal the structure of the supercell (mesoscale unit cell) by using its periodic arrangement within the superlattice from a single reciprocal space map. The images are extracted without prior knowledge and can perhaps benchmark and inform physical hypotheses in phase-field modeling, first-principle calculations, and molecular dynamics simulations. Distinct from nanobeam diffraction widely used to extract two-dimensional (2D) and three-dimensional (3D) strain in thin films (3, 39), our method produces higher-resolution images and requires no beam focusing or spatial scanning, significantly reducing data acquisition time and thereby enabling the investigation of dynamics at fast timescales.

The recent advances in atomic deposition techniques allow synthesizing high-quality crystals of complex oxides with nanoscale spatial heterogeneity, which generate stunning diffraction patterns resembling those measured with coherent X-ray beams from single-crystalline particles in Bragg coherent diffractive imaging (20). One such system is the multilayer $(PbTiO_3)_n/(SrTiO_3)_n$ (40), with an optically induced coherent 3D supercrystal phase (4). The superlattice is revealed by the X-ray diffraction pattern around the 004 $DyScO_3$ substrate (DSO) pseudo-cubic Bragg peak of $(PbTiO_3)_{16}/(SrTiO_3)_{16}$ multilayer system, in which evenly spaced off-specular satellite peaks emerge within the reciprocal cross-section along $Q_z \| [110]_{DSO}$ and $Q_x \| [\bar{1}\ 10]_{DSO}$ (see Fig. 2*A*). Due to the Fourier slice theorem, the shown cross-section $I(Q_x, Q_z)$ is the squared magnitude of the Fourier transform of the projection of the structure in the Q_y direction: it represents a cross-sectional view of the film along the substrate surface in the $[001]_{DSO}$ direction.

To phase the diffraction data, $I(Q_x, Q_z)$, we use a conventional 2D phase retrieval algorithm (see the details on the algorithm and the selection of support in *Methods*) (36). Fig. 2*B* shows the calculated squared magnitude of the Fourier transform of the structure, retrieved through an iterative algorithm from the data (see Fig. 2*A*) initiated with a fully randomized guess. The reconstruction successfully reproduces the main features of the measured diffraction data, such as the satellite peaks and the Laue fringes in between (compare Fig. 2 *A* and *B*). Akin to Bragg coherent diffractive imaging (20), the retrieved image, $\rho(x,z) = s(x,z)\exp\left[i\ \vec{Q}\cdot\vec{u}(x,z)\right]$, consists of the electron density of Bragg planes, $s(x,z)$, and the displacement field projected along the measured reciprocal space vector, $\vec{Q}\cdot\vec{u}(x,z) = Q_z u_z(x,z)$. Fig. 2*C* shows the retrieved displacement field, $u_z(x,z)$ (along Q_{004}), used to calculate X-ray data in Fig. 2*B*. A 2D periodicity is apparent. Moreover, calculating the derivative of the vertical displacement field $u_z(x,z)$ along the vertical direction, z, yields normal strain (NS), and along the horizontal direction, x, yields the local crystal-plane inclination (CI) of the lattice planes (see *Methods*). The NS and CI maps (see Fig. 2 *D* and *E*) reveal the object to be a stack of alternating horizontal layers with a half-period offset in the horizontal direction.

A critical consistency test of phase retrieval is the averaging over multiple runs of the algorithm initiated by random starting conditions (15, 21, 25, 36, 41). A reconstruction is successful when the squared modulus of the Fourier transform of the average real-space image closely resembles the measured intensity, which requires all runs of the algorithm to converge to a unique real-space solution. This requirement is not fulfilled here. All real-space images display patches of short-range-ordered 2D checkerboard texture; nevertheless, the area and position of periodic regions are inconsistent across the differently initialized phase retrieval runs, preventing us from efficient averaging (only 100 out of 2,000 individual reconstructions display a high mutual correlation, see *SI Appendix*, Fig. S1). Indeed, the variation in the long-range order is unsurprising: the data collected with partially coherent, unfocused X-rays lack the interference between the multiple illuminated areas on the film (either due to the low spatial X-ray coherence or the interference fringes being much smaller than the detector pixel size) (42).

Despite the failure of the conventional averaging, we extract the characteristic structural motifs of the short-range order by applying unsupervised machine learning to the set of reconstructed

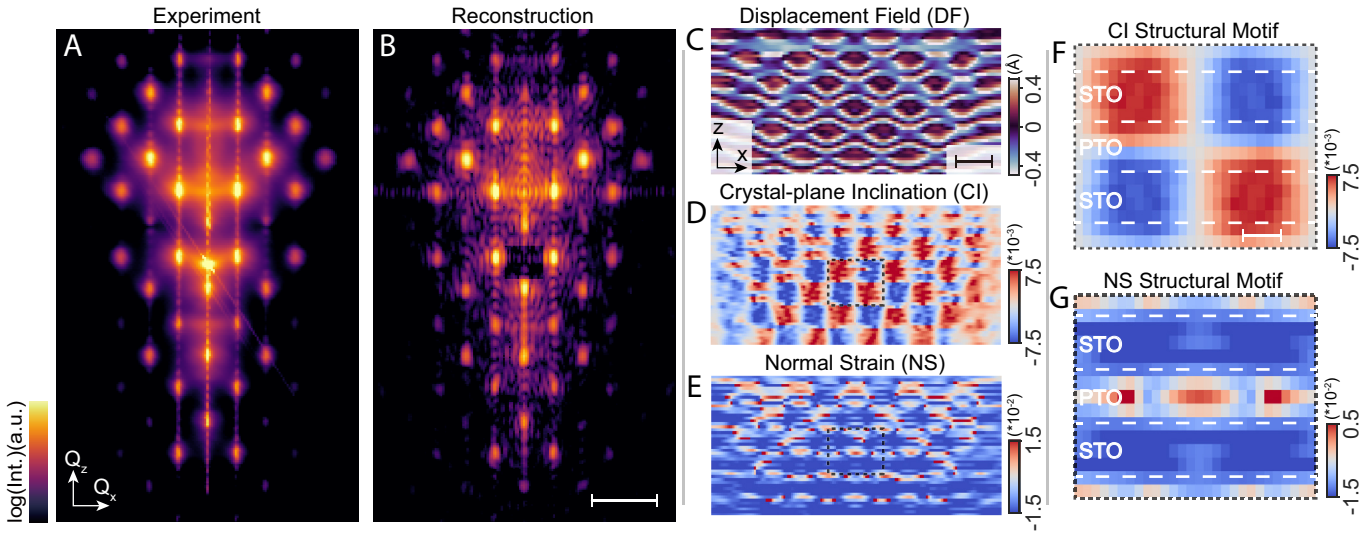

Fig. 2. Real-space imaging of the $(PbTiO_3)_{16}/(SrTiO_3)_{16}$ superlattice. (*A*) Experimentally measured X-ray diffraction data and (*B*) a typical diffraction pattern reconstructed through iterative phase retrieval from a randomized initialization (shown in logarithmic scale). The reconstructed pattern in *B* is the squared Fourier magnitude of the real-space object with a displacement field shown in *C*. The distinct 2D periodic features in the experimental diffraction pattern are reproduced by the reconstruction. The central sharp peak in the measured pattern corresponding to the $DyScO_3$ substrate is removed for the iterative phase retrieval. Real-space images of the (*C*) displacement field (DF), (*D*) crystal-plane inclination (CI), and (*E*) normal strain (NS) extracted from the data in *A*. Real-space images of the (*F*) CI and (*G*) NS of the characteristic structural motif found through unsupervised machine learning from 2,000 independent reconstructions with different random initializations (*C*–*E*). The supercell has a size of 25.3 nm and 30.3 nm in the vertical and horizontal directions, respectively. The scale bar in *B* is 0.05 $Å^{-1}$, in *C* is 20 nm, and in *F* is 5 nm.

structures. First, we define a periodic mesoscale unit cell, the supercell, and determine its period in x and z directions (p_x, p_z) from the satellite peak positions in the diffraction data. We determine the supercell locations by cross correlating the CI with a test function, $\sin(2\pi x/p_x) \cdot \sin(2\pi z/p_z)$. We then partition $2 \cdot 10^3$ images of CI (see Fig. 2*D*) into an ensemble of $2.2 \cdot 10^4$ supercells of size $p_x \cdot p_z$. Finally, we classify and label the supercells through k-means clustering and call the distinct averaged supercell structural motifs (SMs) (see *SI Appendix*, Figs. S2 and S3). Fig. 2 *F* and *G* shows the CI and the NS maps of the most dominant structural motif. As expected from the synthesis, the NS map shows the bilayer with a larger (smaller) lattice constant of $PbTiO_3$ ($SrTiO_3$). The CI map reveals patches of up tilt (red) and down tilt (blue), when following the crystal planes from left to right. The imaging is consistent with the phase-field modeling presented in the original publication (4) and reveals additional features, including the impact of the CI on the lattice constant (tensile strain between tilt-up and tilt-down regions in the $SrTiO_3$ layer) (*SI Appendix*, Fig. S4).

Having demonstrated the combination of iterative phase retrieval with unsupervised machine learning on a previously studied system, we use it to investigate the impact of strain on the Mott transition in Ca_2RuO_4—an important member of the strongly correlated material family with a wide variety of electronic and magnetic phenomena. Notably, Ca_2RuO_4 features a Mott metal–insulator transition, which strongly couples to a structural transition from high-temperature L-Pbca phase to low-temperature S-Pbca phase (43–46). Ca_2RuO_4 thin films have been successfully grown upon various substrates, and the metal-to-insulator transition temperature has been tuned by biaxial in-plane epitaxial strain (47–49). When grown on $LaAlO_3$ (LAO), instead of the abrupt resistivity change at 357 K observed in bulk Ca_2RuO_4 (45), the metal–insulator transition broadens in temperature, and the transition temperature reduces to 230 K, revealed by the change in the sign of dR/dT (resistance (R), temperature (T), see Fig. 3*A*). The suppressed metal–insulator transition temperature has been ascribed to the compressive epitaxial strain, which impedes the expansion of the Ca_2RuO_4 lattice within the *ab* basal plane during the accompanying structural transition (see Fig. 3*B*) (47).

To achieve a better understanding of the structural behavior during the Mott transition in strained Ca_2RuO_4, we collected X-ray diffraction reciprocal space maps at 300 K (metal) and 7 K (insulator) around the 008 Bragg peak of a 17-nm-thick Ca_2RuO_4 film epitaxially grown on $LaAlO_3$ substrate (see Fig. 3*C*). Above the transition temperature, a sharp Bragg peak with Laue fringes indicates the excellent quality of the Ca_2RuO_4 thin film. Below the transition temperature, additional satellite peaks emerge perpendicular to $Q_z \| [001]_{LAO}$. The satellite peaks are confined to two orthogonal planes Q_x–Q_z and Q_y–Q_z, where $Q_x \| [110]_{LAO}$ (Fig. 3*D*, *i*–*iii*). The line profile along Q_x (or Q_y, not shown) at Q = 006, 008, and 0014 displays evenly spaced satellite peaks with a position in Q_x independent of the Bragg peak (see Fig. 3*E*, *i*–*iii*), indicating nanoscale periodicity in the Ca_2RuO_4 film as the origin of satellite peaks instead of lattice tilting. A tilting of large domains would lead to larger satellite distances in Q_x at higher momentum transfer Q_z (50). We estimate the corresponding periodic length as $2\pi / \Delta q \approx 17.5$ nm (Δq = distance between satellite peaks along Q_x), which is temperature independent (*SI Appendix*, Fig. S5). Moreover, we observe a peak broadening by comparing the 1st-, 2nd-, and 3rd-order satellite peaks in the Q_x direction, suggesting slight period length variations between different patches of short-order domains.

The diffraction pattern of the 008 peak at 7 K in the Q_x–Q_z plane shows high-quality interference fringes with multiple satellites present symmetrically in both directions (see Fig. 4*A*), suggesting an intricate superlattice structure. Because all satellite peaks are confined to two distinct planes (Q_x–Q_z or Q_y–Q_z), we conclude that they emerge from two spatially distinct types of nanotextures (*SI Appendix*, Fig. S6), oriented perpendicularly to each other (indistinguishable by the symmetry of the substrate). Diffraction confined to the Q_x–Q_z plane suggests nanoscale heterogeneity in the x–z plane, extended over a larger length in the y-direction. The diagonal streaks in the diffraction data in the Q_x–Q_z plane further indicate structural motifs with diagonally oriented boundaries in the x–z plane of the real-space structure.

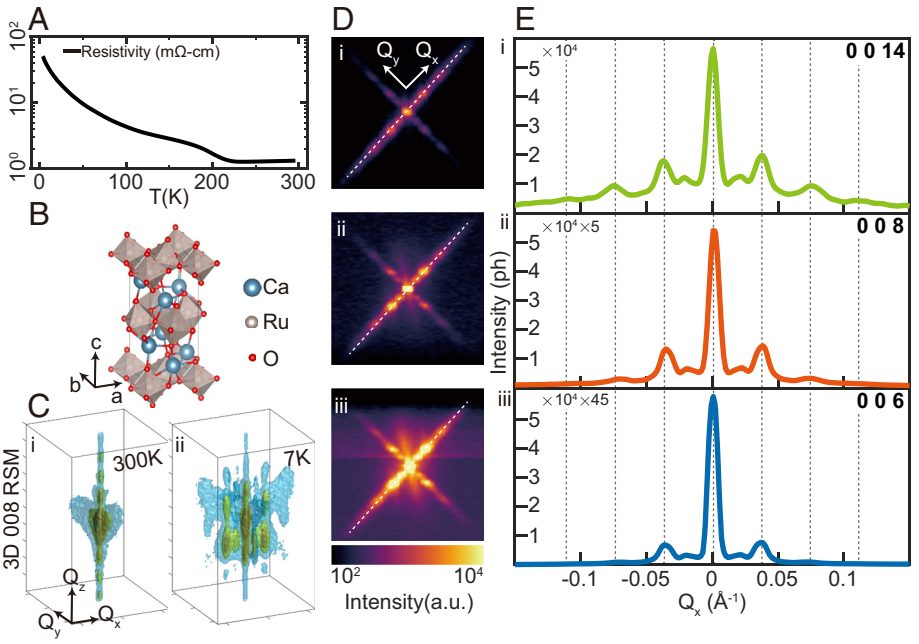

Fig. 3. X-ray satellite peaks in strained Ca_2RuO_4 thin film induced by the metal-to-insulator transition. (*A*) The resistivity of the compressively strained 17 nm Ca_2RuO_4 film grown on $LaAlO_3$ (LAO) as a function of temperature. A metal-to-insulator transition occurs around 230 K. (*B*) Structure of the Ca_2RuO_4 L-Pbca lattice. (*C*) 3D reciprocal space maps (RSMs) around the 008 peak of the Ca_2RuO_4 thin film at 300 K (*i*) and 7 K (*ii*) ($Q_z \| c \| [001]_{LAO}$, $Q_x \| a \| [110]_{LAO}$, $Q_y \| b \| [\bar{1}10]_{LAO}$). The satellite peaks visible at 7 K induced by the metal-to-insulator transition are absent at 300 K. (*D*) Projection of the RSMs measured at 7 K along Q_z around 0014 (*i*), 008 (*ii*), 006 (*iii*) peaks. (*E*) Intensity line profiles of the diffraction pattern along the dashed line in (*D*). The satellite peak spacing is constant across multiple Bragg peaks, indicating mesoscale periodicity as the origin of satellite peaks.

A typical diffraction pattern found through iterative phase-retrieval algorithm with a randomized starting guess reproduces most of the features in the measured data, including the diagonally placed satellite peaks and their relative intensities (compare Fig. 4 *A* and *B*). The displacement field of the corresponding real-space structure exhibits a continuous periodic zig-zag-shaped modulation (*SI Appendix*, Fig. S7). The zig-zag pattern comprises diagonally oriented interfaces consistent with diagonal streaks in the diffraction pattern. Inspecting the individual phase retrieval reconstructions with different random initializations, one notices the presence of a similar in-plane periodicity with various types of supercells, all reproducing the measured diffraction pattern (*SI Appendix*, Fig. S7). Yet, only 200 out of 2,000 reconstructions display a high correlation, again preventing us from conventional averaging.

We identify four characteristic structural motifs (SM1-SM4) composing the short-range order observed in the set of 2,000 reconstructions. The features are well resolved in our ~14 nm × 18 nm large real-space images with a pixel size of ~2 nm × 1 nm. For SM1 and SM2, the NS maps show a triangular structure with a smaller *c*-axis lattice constant (see Fig. 4*C*, *i* and *ii*). The corresponding CI maps show a cross shape with different crystal-plane inclinations (see Fig. 4*D*, *i* and *ii*). For SM3 and SM4, a 6-nm-wide diagonal stripe is visible in the NS maps (see Fig. 4*C*, *iii* and *iv*) and in the corresponding CI maps (see Fig. 4*D*, *iii* and *iv*). The presence of the structural motifs is restricted by the reflection symmetry observed in the measured diffraction pattern along the vertical axis. Although SM3 and SM4 have no reflection symmetry within themselves, they are mirror reflections of each other and have an identical population, enabling them to collectively generate a symmetric pattern. In contrast, SM1 and SM2 are symmetric with respect to their central vertical lines (see the displacement field in *SI Appendix*, Fig. S9), allowing them to produce symmetric diffraction patterns independently. Notably, as SM1 and SM2 are the point reflections of each other, the possibility that SM1 and SM2 are related by Friedel's law cannot be excluded. Nevertheless, the concurrent presence of SM1 and SM2 in a single reconstruction has not been observed (see *SI Appendix*, Fig. S7).

To confirm the validity of our X-ray imaging, we performed cryogenic high-angle annular dark-field (HAADF) scanning transmission electron microscopy (STEM) at ~100 K on the cross-section of a similar ~34 nm-thick $Ca_2RuO_4/LaAlO_3$ film. Fig. 4*D* shows a map of the local interplanar spacing along the $[001]_{LAO}$ direction extracted from the atomic resolution HAADF-STEM images, which confirms the presence of mirrored diagonal features similar to those visible in the reconstructed SM3 and SM4. Some mirrored diagonals overlap, forming triangular patterns akin to SM1 and SM2 in our X-ray imaging. In addition to the similar morphology, the angle of the diagonal interfaces in the STEM measurement is ~48°, which matches the angle observed in our X-ray imaging (see Fig. 4*D*, *iv*) as well as the angle for the lowest-energy S-Pbca/L-Pbca interface. Although the Ca_2RuO_4 film shows local mesoscale periodicity, variations in the short-range order are present, and a long-range regular strain ordering is not observed within the STEM measurement.

The striped nanotexture of the epitaxially strained Ca_2RuO_4 thin film revealed by the real-space imaging likely results from elastic energy minimization, similar to the formation of nanotextures in other complex oxides (4). The nanotexture has not been reported in bulk Ca_2RuO_4, suggesting that epitaxial strain stabilizes it. The nanotexture disappears at high temperatures above the Mott transition and reappears at low temperatures in the Mott state, creating an exciting opportunity for controlling the nanotexture by Mott physics. The out-of-plane lattice constant of alternating stripes indicates that the two structures are derivatives of the high-temperature metallic L-Pbca phase and low-temperature insulating S-Pbca phase. Nevertheless, spatially resolved studies—such as near-field optical nanoscopy (7), resonant scanning X-ray microscopy, or energy-resolved electron microscopy—are needed to better understand the correlation of the observed structural

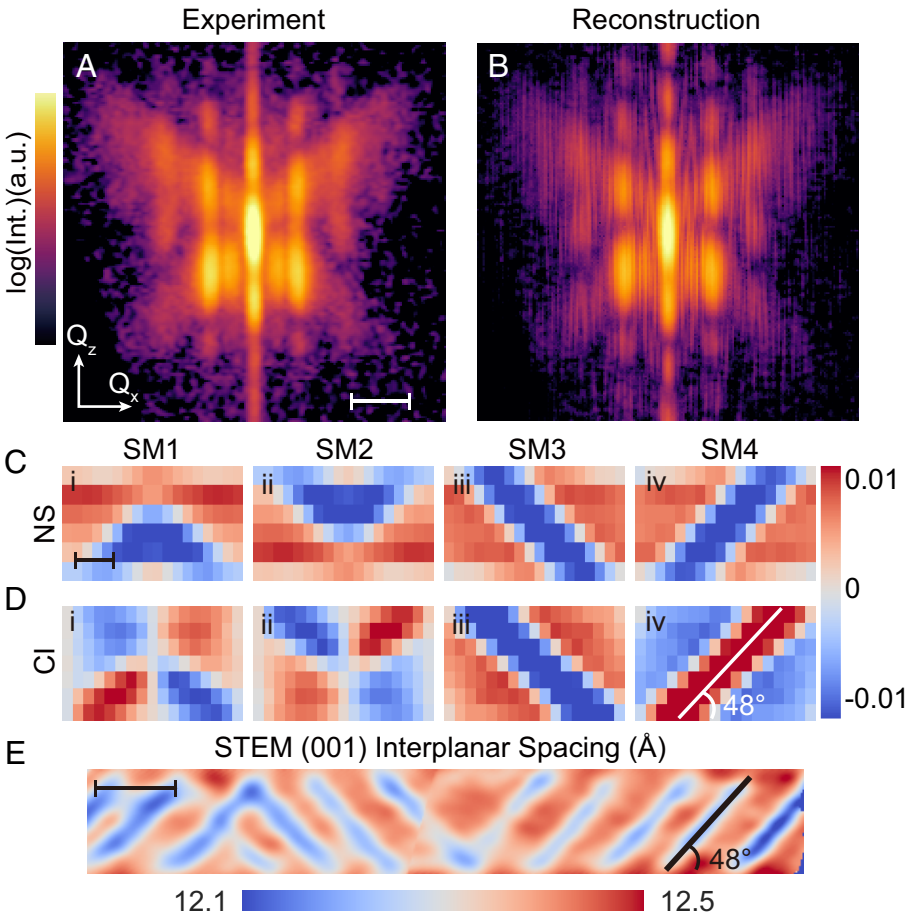

Fig. 4. Real-space imaging of the nanotexture emerging during the metal-to-insulator transition in a strained Ca_2RuO_4 thin film. (*A*) Measured and (*B*) reconstructed diffraction pattern near the 008 peak of Ca_2RuO_4 thin film at 7 K (shown in logarithmic scale). The slice shown in *A* is taken along the dashed white line in Fig. 3*D*. The reconstructed diffraction pattern in *B* is the squared Fourier magnitude of the real-space object with a displacement field shown in *SI Appendix*, Fig. S7. Through iterative phase retrieval and unsupervised machine learning, we identify four characteristic structural motifs (SMs). (*C* and *D*) Real-space images of (*C*) normal strain (NS) and (*D*) crystal-plane inclination (CI) in the corresponding structural motifs. The structural motifs shown have a size of ~14 nm × 18 nm. The population of the supercells with the four different structural motifs has a ratio of ~2:2:1:1. (*E*) A map of the interplanar spacing along [001] extracted from HAADF-STEM images of the cross-section of a ~34-nm-thick Ca_2RuO_4 film at ~100 K on the $[110]_{LAO}$ zone axis. Both zig-zag and diagonal stripe patterns are observed in the image. The average angle of the stripes is close to 48°, which coincides with the angle determined from the X-ray images (see *C* and *D*). The scale bar in *A* is 0.05 $Å^{-1}$, in *C* is 5 nm, and in *E* is 20 nm.

texture with local charge, spin, and orbital ordering. An exciting future direction is studying and understanding the femtosecond-to-picosecond dynamic evolution of the nanotexture in Mott insulators such as Ca_2RuO_4 because of the excitations and timescales that can form due to the periodicity.

In summary, we demonstrated the real-space imaging of the periodic structural nanotexture in $(PbTiO_3)_{16}/(SrTiO_3)_{16}$ superlattice and Ca_2RuO_4 epitaxial thin films through the combination of iterative phase retrieval and unsupervised machine learning. In the first step, the phase retrieval algorithm identifies an ensemble of possible real-space arrangements that are consistent with the X-ray data; in the second step, machine learning finds a meaningful subset of structural motifs within these arrangements. Our model-independent X-ray imaging approach agrees with the phase-field modeling in $(PbTiO_3)_{16}/(SrTiO_3)_{16}$ and cryogenic scanning transmission electron microscopy measurement results in Ca_2RuO_4. The real-space images of nanotexture structural motifs represent averages over millimeter-large, multidomain areas. The success of the approach, therefore, requires a nanotexture with uniform periodicity over extended areas. The recent developments in atomic deposition technologies make the technique highly applicable in visualizing the ubiquitous nanotextures in low-dimensional quantum materials and microelectronics, often displaying so-called "butterfly" or more complex diffraction patterns (2, 4, 34, 35). The averaging over extensive areas highlights our technique's complementarity with local imaging probes such as Bragg coherent diffractive imaging, ptychography, and atomic-resolution electron microscopy, all limited to relatively small film areas and potentially prone to local defects. Furthermore, the approach is applied without extensive sample preparation, which might modify the strain state or let the metastable state relax into a more stable configuration (51). Because the imaging is nonperturbative, its extension to in-situ and ultrafast experiments at X-ray free-electron lasers appears straightforward. Finally, the combination of iterative phase retrieval and machine learning is a potential pathway to invert data with nonunique solutions, and we anticipate that the combination of our approach with more sophisticated phase retrieval algorithms, for example, using the multimodal approach (26, 52), will allow studying more complex systems with coexisting orders.

Materials and Methods

Sample Preparation. The Ca_2RuO_4 thin film was grown in a Veeco GEN10 molecular-beam epitaxy (MBE) system on a $(001)_{pc}$-oriented $LaAlO_3$ substrate from CrysTec GmbH. The film was grown at a substrate temperature of 870 °C as

measured using a pyrometer operating at 1,550 nm. Elemental calcium (99.99% purity) and elemental ruthenium (99.99% purity) were evaporated from a low-temperature effusion cell and an electron beam evaporator, respectively. The films were grown with a calcium flux of 1.8×10^{13} atoms·cm^{-2}s^{-1} and a ruthenium flux of 1.7×10^{13} atoms·cm^{-2}s^{-1} in a background of 7×10^{-7} Torr of ozone (10% O_3 + 90% O_2). At the end of the growth, the shutter on both calcium and ruthenium sources was closed and the sample was cooled down to 250 °C in the same background pressure as used during the growth. The sample thickness of 17 nm was determined by fitting the Laue fringes in Fig. 3*C*, *i* of the main text.

Resistivity Measurement. The resistance is measured with the standard four-probe method, with four electrical contacts attached to the thin film near the corners of a 10 mm × 10 mm wafer. The square edges of the wafer are aligned along the [100] and [010] pseudo-cubic directions of $LaAlO_3$. Resistance is converted to resistivity using van der Pauw's formula for a 17-nm-thick conducting sheet.

X-Ray Diffraction (XRD). The $PbTIO_3$/$SrTiO_3$ (PTO/STO) XRD data are taken from Stoica *et al.* (4). Detailed PTO/STO XRD experimental specifications can be found in the cited work. The Ca_2RuO_4 synchrotron XRD data were measured at A2 beamline of the Cornell High-Energy Synchrotron Source (CHESS) with the incident photon energy of 19.75 keV (wavelength $\lambda = 0.6278$ Å). The beam is unfocused during the diffraction measurement with the approximate illuminate size of ~200 $\mu m \times$ 400 μm on the film. A Pilatus3 300 K-pixel area detector (487 × 619 pixels in an 83.8 mm × 106.5 mm active area) was positioned 574.34 mm from the sample. The 3D reciprocal space around Bragg peaks of interest was acquired by θ -scan (rocking-curve) of the sample, rotating in 320 steps of 0.0125° with one image recorded per step. The acquisition time is 1 s with an average of 2.7×10^5 photons collected for each image.

2D Phase Retrieval Algorithm and Strain imaging. The phase retrieval algorithm implemented in this work is a custom version of the Fienup's output–output (OO) algorithm (36) (code posted in the Supplementary Information). For each reconstruction initialized with a random start, we run 20 mini-iterations, which is composed of 60 OO [0.6] iterations (output–output algorithm with feedback parameter $\beta = 0.6$), then 20 OO [0.8] iterations followed by 20 OO [0.98] iterations in the end. Also, we assume the object we reconstructed is a phase object (i.e., the object amplitude, $s(x, y)$, is constant). We assume the slight modulations in the amplitude intensity to be insignificant for the phase retrieval: in far-field diffraction, the phase information has more contribution to the resulting diffraction pattern compared to the amplitude information of the object (24). A finite rectangular support is used as the real-space constraint. The vertical size of the support is determined by the thickness of the film, determined from thickness fringes in the diffraction pattern. By fine-tuning the vertical support size and comparing the Laue fringes of the corresponding reconstructions with the measured pattern, the optimal vertical support size calculated is 75 nm for PTO/STO and 14 nm for Ca_2RuO_4. Compared to the vertical support size, the horizontal support size is not well defined because the film is homogeneous over millimeters, and the X-ray beam size is on the scale of hundreds of microns. We assume the measured intensity is a sum of intensities from many short-range ordered domains. The interference between separated domains, which should be present if multiple domains were coherently illuminated and the detector resolution was high enough to resolve these small interference fringes, is not visible because of the poor spatial coherence of the X-ray beam and the interference fringes being too small to resolve with the given experimental setup (a situation similar to ref. 42). Therefore, we choose a support size in the horizontal direction mimicking a domain size of the short-range ordered domain. To check the validity of this approach, we tested various sizes of the support in the horizontal direction. Our analysis shows that the horizontal support size has no significant influence on the phase retrieval results and a negligible impact on the structural motifs (compare Fig. 4*C* and *D* with *SI Appendix*, Fig. S12*B*). The horizontal support size selected in this work is the maximum size allowed without violating the oversampling principle, which is 172 nm for PTO/STO and 170 nm for Ca_2RuO_4 reconstruction (horizontal support introduces intensity modulations in the horizontal direction; at least two detector pixels per modulation are required for oversampling. See *SI Appendix*, Fig. S11 for further discussion on support size selection).

After the diffraction pattern is phased by the phase retrieval algorithm, the corresponding real-space complex phase object $\rho(x, z) = s(x, z) \cdot \exp[i\ \varphi(x, z)]$ can be directly inverted by Fourier transform. The real-space phase $\varphi(x, z)$ represents the local atomic displacement from the ideal lattice projected onto the scattering vector at a Bragg condition (15), *i. e.*, $\varphi(x, z) = \vec{Q} \cdot \vec{u}(x, z) = |Q| \cdot u_{\vec{Q}}(x, z)$. The $\vec{Q}$ of the specular Braggs peak in our work is parallel to the z direction (out-of-plane direction of thin film). Therefore, by dividing the phase $\varphi(x, z)$ by $|Q|$, we can get the displacement field (DF) $u_z(x, z)$ of the real space object. Notably, because the cyclic nature of the phase $\varphi(x, z)$ and shifting the phase of the real-space object $\rho(x, z)$ by a constant will make no change to the corresponding diffraction pattern (canceled when calculate squared modulus), there is no physical difference between DF maps with constant cyclic difference, which can be interpreted as viewing the same displacements with different point of references (see *SI Appendix*, Figs. S1*B* and S7*B*). Instead of the indeterministic DF maps, more structural information can be gained by calculating the derivatives of the DF $u_z(x, z)$ with respect to position x or z, leading to crystal-inclination (CI) $\frac{\partial u_z(x,z)}{\partial x} \cdot p_x$ and normal strain (NS) $\frac{\partial u_z(x,z)}{\partial z} \cdot p_z$ maps (p_x and p_z are the pixel size in the corresponding direction). The CI maps describe the local lattice tilting angles resulted from shear strain and relative rotation. The NS maps describe the relative lattice interspacing in z direction, analogous to tensile strain.

Note that a Patterson function approach fails because the measured object is dense (because we only measure signal around one Bragg peak) and complex-valued (because the crystal is distorted and the displacement field leads to asymmetric diffuse scattering around the Bragg peak).

Unsupervised Machine Learning for Determining the Supercell. We first determine the size of the supercell according to the mesoscale periodicity length, which can be calculated from the average of the reconstructed object autocorrelations (Fourier transform of the measured intensity). It's equivalent to determining the size of the supercell from the interspacing of the satellite peaks of the diffraction pattern. For the PTO/STO, the 2D calculated periodicity is $(p_x, p_z) = (30.3\ \text{nm}, 25.3\ \text{nm})$. For the Ca_2RuO_4 thin film, the autocorrelations show no periodicity in the vertical direction. Therefore, we split the real-space reconstructions into supercells arranged in 1D with a calculated periodicity of $p_x = 18.0$ nm. Then, the supercells can be located by finding the local maximum of the crosscorrelation between the individual reconstructions and the sinusoidal test function, which is built with the same size as the supercells. Finally, to separate the collected supercells with different patterns, we cluster the supercells using the square-Euclidean-distance k-means++ algorithm (38) with 1000 initializations and a maximum number of iterations of 10,000. The clustered supercells are subsequently averaged as the characteristic structural motif of that cluster (see *SI Appendix*, Fig. S2). The code required for generating results shown in Fig. 1 is freely available here: https://github.com/ZimingS/Periodic-Textures-Imaging.

Cryogenic Scanning Transmission Electron Microscopy (cryo-STEM). Cryo-STEM characterization was performed on a cross-sectional lamella prepared with the standard focused ion beam (FIB) lift-out procedure using a Thermo Fisher Helios G4 UX FIB. Cryogenic HAADF-STEM imaging was performed on an FEI/Thermo Fisher Titan Themis CryoS/TEM with a Gatan 636 double-tilt liquid nitrogen cooling holder at 300 kV with a 30-mrad convergence semi-angle. For high-precision structural measurements, a series of 20 rapid-frame images (~1.6 s. per frame) were acquired and subsequently realigned and averaged by a method of rigid registration optimized to prevent lattice hops (53), resulting in high signal-to-noise ratio, high-fidelity images of the atomic lattice. The c-axis interplanar spacing was extracted from the HAADF-STEM images using the strain mapping technique developed by Smeaton et al. (54) on the 001 peak of the Ca_2RuO_4 film. To show a sufficient area of the film, two STEM images of overlapping areas of the sample were aligned and montaged together. Unprocessed images and corresponding interplanar spacing maps are shown in *SI Appendix*, Fig. S10.

Data, Materials, and Software Availability. The X-ray reciprocal space mapping data presented in this work are available for download at the Open Science Framework for the Ca_2RuO_4 thin film (https://doi.org/10.17605/OSF.IO/KDYPR) (55) https://doi.org/10.17605/OSF.IO/KDYPR and for the PbTiO3/SrTiO3 superlattice (https://doi.org/10.17605/OSF.IO/XJ8WE) (56). The cryogenic scanning transmission electron microscopy data of the Ca2RuO4 thin film is available for download at The Platform for the Accelerated Realization, Analysis, and Discovery of Interface Materials database (PARADIM) (https://doi.org/10.34863/3tms-hn27)

(57). All data needed to evaluate the conclusions presented are included in the article and/or *SI Appendix*.

ACKNOWLEDGMENTS. The work was primarily supported by U.S. Department of Energy, Office of Science, Office of Basic Energy Sciences, under contract no. DE-SC0019414 (development of the phase retrieval algorithm, data analysis, and interpretation: Z.S., O.Y.G., D.G.S., K.M.S., A.S.; thin-film synthesis: H.N.). This research was funded in part by the Gordon and Betty Moore Foundation's EPiQS Initiative through grant nos. GBMF3850 and GBMF9073 to Cornell University. Sample preparation was, in part, facilitated by the Cornell NanoScale Facility, a member of the National Nanotechnology Coordinated Infrastructure (NNCI), which is supported by the NSF (grant no. NNCI-2025233). We thank Benjamin Gregory for careful reading of the manuscript. Research conducted at CHESS was supported by the NSF (BIO, ENG and MPS Directorates) under awards DMR-1332208 and DMR-1829070. Use of the Advanced Photon Source was supported by DOE's Office of Science under contract DE-AC02-06CH11357. Transmission electron microscopy work was supported by the NSF [Platform for the Accelerated Realization, Analysis, and Discovery of Interface Materials (PARADIM)] under Cooperative Agreement No. DMR-2039380 and made use of the Cornell Center for Materials Research Shared Facilities, which are supported through the NSF MRSEC program (DMR-1719875). N.S. was supported by the NSF Graduate Research Fellowship (DGE-2139899). B.H.G. was supported by PARADIM (NSF DMR-2039380). L.F.K. acknowledges support by the Packard Foundation. T.Y. and L.-Q.C.'s efforts on phase-field simulations are supported as part of the Computational Materials Sciences Program funded by the U.S. Department of Energy, Office of Science, Basic Energy Sciences, under award no. DE-SC0020145. C.D.'s effort is supported by the U.S. Department of Energy, Office of Science, Office of Basic Energy Sciences, under award number DE-SC-0012375. V.A.S. and J.W.F. acknowledge the U.S. Department of Energy, Office of Science, Office of Basic Energy Sciences, under award number DE-SC-0012375, for support in studying complex-oxide heterostructure with X-ray scattering.

Author affiliations: [a]Department of Materials Science and Engineering, Cornell University, Ithaca, NY 14853; [b]Department of Physics, Cornell University, Ithaca, NY 14853; [c]Department of Materials Science and Engineering, Pennsylvania State University, University Park, PA 16802; [d]School of Applied and Engineering Physics, Cornell University, Ithaca, NY 14853; [e]Kavli Institute at Cornell for Nanoscale Science, Cornell University, Ithaca, NY 14853; [f]Advanced Photon Source, Argonne National Laboratory, Lemont, IL 60439; [g]Cornell High Energy Synchrotron Source, Cornell University, Ithaca, NY 14853; and [h]Leibniz-Institut für Kristallzüchtung, Berlin 12489, Germany

1. J. H. Haeni *et al.*, Room-temperature ferroelectricity in strained SrTiO3. *Nature* **430**, 758–761 (2004).
2. G. Catalan *et al.*, Flexoelectric rotation of polarization in ferroelectric thin films. *Nat. Mater* **10**, 963–967 (2011).
3. A. Singer *et al.*, Nonequilibrium phase precursors during a photoexcited insulator-to-metal transition in V2 O3. *Phys. Rev. Lett.* **120**, 207601 (2018).
4. V. A. Stoica *et al.*, Optical creation of a supercrystal with three-dimensional nanoscale periodicity. *Nat. Mater* **18**, 377–383 (2019).
5. X. Chen *et al.*, Moiré engineering of electronic phenomena in correlated oxides. *Nat. Phys.* **16**, 631–635 (2020).
6. D. v. Christensen *et al.*, Strain-tunable magnetism at oxide domain walls. *Nat. Phys.* **15**, 269–274 (2019).
7. A. S. McLeod *et al.*, Nanotextured phase coexistence in the correlated insulator v 2 O 3. *Nat. Phys.* **13**, 80–86 (2017).
8. X. Ke, M. Zhang, K. Zhao, D. Su, Moiré fringe method via scanning transmission electron microscopy. *Small Methods* **6**, 2101040 (2022).
9. A. Tselev *et al.*, Interplay between ferroelastic and metal-insulator phase transitions in strained quasi-two-dimensional VO2 nanoplatelets. *Nano Lett.* **10**, 2003–2011 (2010).
10. Q. Li *et al.*, Ferroelastic nanodomain-mediated mechanical switching of ferroelectricity in thick epitaxial films. *Nano Lett.* **21**, 445–452 (2021).
11. V. Petrícek, M. Dušek, L. Palatinus Crystallographic computing system JANA2006: General features. *Zeitschrift fur Kristallographie* **229**, 345–352 (2014), https://doi.org/10.1515/zkri-2014-1737.
12. Y. Yacoby *et al.*, Direct determination of epitaxial interface structure in Gd 2O3 passivation of GaAs. *Nat. Mater* **1**, 99–101 (2002).
13. M. D. Collins, G. Hummer, M. L. Quillin, B. W. Matthews, S. M. Gruner, *Cooperative water filling of a nonpolar protein cavity observed by high-pressure crystallography and simulation*. (2005). www.pnas.orgcgidoi10.1073pnas.0508224102. Accessed 1 January 2023.
14. B. E. Warren, *Warren X-ray Diffraction* (Courier Dover Publications, New York, 1969).
15. I. Robinson, R. Harder, Coherent X-ray diffraction imaging of strain at the nanoscale. *Nat. Mater* **8**, 291–298 (2009).
16. D. Sayre, Some implications of a theorem due to Shannon. *Acta Crystallogr.* **5**, 843–843 (1952).
17. D. Sayre, Prospects for long-wavelength X-ray microscopy and diffraction. *Imaging Processes Coherence Phys.* **285**, 229–235, (2008), 10.1007/3-540-09727-9_82.
18. J. Miao, P. Charalambous, J. Kirz, D. Sayre, Extending the methodology of X-ray crystallography to non-crystalline specimens. *AIP Conf. Proc.* **521**, 3–6 (2000).
19. H. N. Chapman *et al.*, High-resolution ab initio three-dimensional x-ray diffraction microscopy. *J. Optical Soc. Am. A* **23**, 1179 (2006).
20. M. A. Pfeifer, G. J. Williams, I. A. Vartanyants, R. Harder, I. K. Robinson, Three-dimensional mapping of a deformation field inside a nanocrystal. *Nature* **442**, 63–66 (2006).
21. H. N. Chapman, K. A. Nugent, Coherent lensless X-ray imaging. *Nat. Photonics* **4**, 833–839 (2010).
22. J. A. Rodriguez, R. Xu, C. C. Chen, Y. Zou, J. Miao, Oversampling smoothness: An effective algorithm for phase retrieval of noisy diffraction intensities. *J. Appl. Crystallogr.* **46**, 312–318 (2013).
23. P. Thibault *et al.*, High-resolution scanning x-ray diffraction microscopy. *Science* **321**, 379–382 (2008).
24. K. A. Nugent, Coherent methods in the X-ray sciences. *Adv. Phys.* **59,** 1–99 (2010).
25. I. A. Vartanyants, I. K. Robinson, Partial coherence effects on the imaging of small crystals using coherent x-ray diffraction. *J. Phys. Condensed Mat.* **13**, 10593–10611 (2001).
26. L. W. Whitehead *et al.*, Diffractive imaging using partially coherent X rays. *Phys. Rev. Lett.* **103**, 1–4 (2009).
27. J. Nelson *et al.*, High-resolution x-ray diffraction microscopy of specifically labeled yeast cells. *Proc. Natl. Acad. Sci. U.S.A.* **107**, 7235–7239 (2010).
28. T. Latychevskaia, H.-W. Fink, Three-dimensional double helical DNA structure directly revealed from its X-ray fiber diffraction pattern by iterative phase retrieval. *Opt. Express* **26**, 30991 (2018).
29. G. J. Williams, M. A. Pfeifer, I. A. Vartanyants, I. K. Robinson, Three-dimensional imaging of microstructure in au nanocrystals. *Phys. Rev. Lett.* **90**, 4 (2003).
30. A. Singer *et al.*, Nucleation of dislocations and their dynamics in layered oxide cathode materials during battery charging. *Nat. Energy* **3**, 641–647 (2018).
31. J. N. Clark *et al.*, Three-dimensional imaging of dislocation propagation during crystal growth and dissolution. *Nat. Mater* **14**, 780–784 (2015).
32. M. M. Seibert *et al.*, Single mimivirus particles intercepted and imaged with an X-ray laser. *Nature* **470**, 78–82 (2011).
33. K. Ayyer *et al.*, Macromolecular diffractive imaging using imperfect crystals. *Nature* **530**, 202–206 (2016).
34. M. Schmidbauer, D. Braun, T. Markurt, M. Hanke, J. Schwarzkopf, Strain engineering of monoclinic domains in K x Na1-xNbO3 epitaxial layers: A pathway to enhanced piezoelectric properties. *Nanotechnology* **28**, 24LT02 (2017).
35. D. D. Fong *et al.*, Ferroelectricity in ultrathin perovskite films. *Science* **1979**, 1650–1653 (2004).
36. J. R. Fienup, Phase retrieval algorithms: A comparison. *Appl. Opt.* **21**, 2758 (1982).
37. S. P. Lloyd, Least squares quantization in PCM. *IEEE Trans. Inf. Theory* **28**, 129–137 (1982).
38. D. Arthur, S. Vassilvitskii, "K-means++: The advantages of careful seeding" in *Proceedings of the Annual ACM-SIAM Symposium on Discrete Algorithms* (2007), pp. 1027–1035.
39. M. Holler *et al.*, High-resolution non-destructive three-dimensional imaging of integrated circuits. *Nature* **543**, 402–406 (2017).
40. A. K. Yadav *et al.*, Observation of polar vortices in oxide superlattices. *Nature* **530**, 198–201 (2016).
41. A. Singer *et al.*, Domain morphology, boundaries, and topological defects in biophotonic gyroid nanostructures of butterfly wing scales. *Sci. Adv.* **2**, e1600149 (2016).
42. O. M. Yefanov *et al.*, Coherent diffraction tomography of nanoislands from grazing-incidence small-angle x-ray scattering. *Appl. Phys. Lett.* **94**, 2–4 (2009).
43. M. Braden, G. André, Crystal and magnetic structure of magnetoelastic coupling and the metal-insulator transition. *Phys. Rev. B* **58**, 847–861 (1998).
44. O. Friedt *et al.*, Structural and magnetic aspects of the metal-insulator transition in Ca2-xSrxRuO4. *Phys. Rev. B* **63**, 1744321–17443210 (2001).
45. C. S. Alexander *et al.*, Destruction of the Mott insulating ground state of Ca2RuO4 by a structural transition. *Phys. Rev. B* **60**, R8422–R8425 (1999).
46. K. Jenni *et al.*, Evidence for current-induced phase coexistence in Ca2RuO4 and its influence on magnetic order. *Phys. Rev. Mater* **4**, 85001 (2020).
47. L. Miao *et al.*, Itinerant ferromagnetism and geometrically suppressed metal-insulator transition in epitaxial thin films of Ca 2RuO 4. *Appl. Phys. Lett.* **100**, 10–13 (2012).
48. C. Dietl *et al.*, Tailoring the electronic properties of Ca2RuO4 via epitaxial strain. *Appl. Phys. Lett.* **112**, 1–6 (2018).
49. A. Tsurumaki-Fukuchi *et al.*, Stable and tunable current-induced phase transition in epitaxial thin films of Ca 2 RuO 4. *ACS Appl. Mater Interfaces* **12**, 28368–28374 (2020).
50. U. Gebhardt *et al.*, Formation and thickness evolution of periodic twin domains in manganite films grown on SrTiO3(001) substrates. *Phys. Rev. Lett.* **98**, 1–4 (2007).
51. D. Pesquera *et al.*, Beyond substrates: Strain engineering of ferroelectric membranes. *Adv. Mat.* **32**, 1–9 (2020).
52. P. Thibault, A. Menzel, Reconstructing state mixtures from diffraction measurements. *Nature* **494**, 68–71 (2013).
53. B. H. Savitzky *et al.*, Image registration of low signal-to-noise cryo-STEM data. *Ultramicroscopy* **191**, 56–65 (2018).
54. M. A. Smeaton *et al.*, Mapping defect relaxation in quantum dot solids upon in situ heating. *ACS Nano* **15**, 719–726 (2021).
55. Z. Shao *et al.*, The X-ray diffraction reciprocal space mapping data of the Ca2RuO4 thin film for "Real-space imaging of periodic nanotextures in thin films via phasing of diffraction data." Open Science Framework. https://doi.org/10.17605/OSF.IO/KDYPR. Deposited 19 May 2023.
56. V. A. Stoica *et al.*, The X-ray diffraction reciprocal space volumes for PbTiO3/SrTiO3 for "Real-space imaging of periodic nanotextures in thin films via phasing of diffraction data" and "Optical creation of a super crystal with three-dimensional nanoscale periodicity" (reference 4). Open Science Framework. https://doi.org/10.17605/OSF.IO/XJ8WE. Deposited 17 June 2023.
57. N. Schnitzer *et al.*, The cryogenic scanning transmission electron microscopy data of the Ca2RuO4 thin film for "Real-space imaging of periodic nanotextures in thin films via phasing of diffraction data." The Platform for the Accelerated Realization, Analysis, and Discovery of Interface Materials (PARADIM). https://doi.org/10.34863/3tms-hn27. Deposited 20 June 2023.

Supporting Information for

Real-space imaging of periodic nano-textures in thin films via phasing of diffraction data

Ziming Shao[1], Noah Schnitzer[1], Jacob Ruf[2], Oleg Y. Gorobtsov[1], Cheng Dai[3], Berit H. Goodge[4,5], Tiannan Yang[3], Hari Nair[1], Vlad A. Stoica[3,6], John W. Freeland[6], Jacob Ruff[7], Long-Qing Chen[3], Darrell G. Schlom[1,5,8], Kyle M. Shen[2,5], Lena F. Kourkoutis[4,5], Andrej Singer[1]

[1]Department of Materials Science and Engineering, Cornell University, Ithaca, NY 14853, USA

[2]Department of Physics, Cornell University, Ithaca, NY 14853, USA

[3]Department of Materials Science and Engineering, Pennsylvania State University, University Park, PA 16802, USA

[4]School of Applied and Engineering Physics, Cornell University, Ithaca, NY 14853, USA

[5]Kavli Institute at Cornell for Nanoscale Science, Cornell University, Ithaca, NY 14853, USA

[6]Advanced Photon Source, Argonne National Laboratory, Argonne, IL 60439, USA

[7]Cornell High Energy Synchrotron Source, Cornell University, Ithaca, NY 14853, USA

[8]Leibniz-Institut für Kristallzüchtung, Max-Born-Straße 2, 12489 Berlin, Germany

* Corresponding author. Email: asinger@cornell.edu

This file includes:

Figs. S1 to S12

Sample code

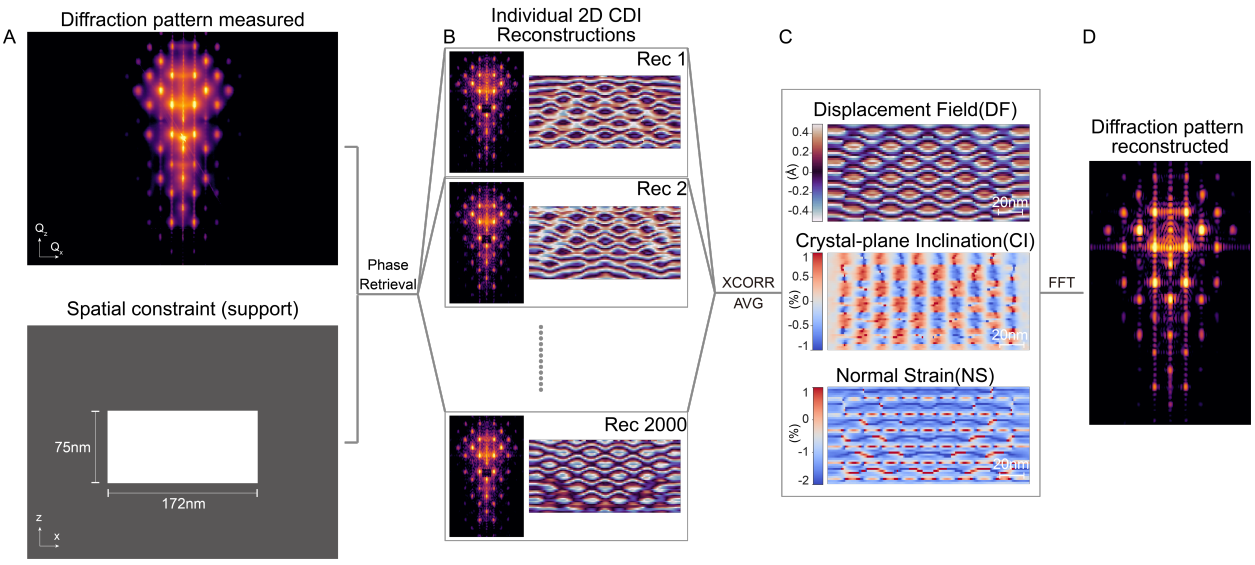

Fig. S1. Phase retrieval and individual reconstructions of $(PbTiO_3)_{16}/(SrTiO_3)_{16}$ (PTO/STO). (**A**) Reciprocal Space Mapping around 004_{pc} Bragg peak of PTO/STO superlattice upon DSO substrate (*1*) (top) and the finite rectangular spatial constraint (support) used in phase retrieval (bottom). (**B**) The diffraction pattern and the corresponding real-space phase object of typical iterative phase retrieval reconstruction with independent randomized initializations. Most features of the measured pattern are well reproduced in reconstructed pattern except the sharp DSO substrate peak in the middle, which was intentionally neglected in the iterative phase retrieval. Periodic-patterned patches with area and location variations are observed within the real-space phase objects. The periodic patches are more likely to be observed in the central region than the edge and corner of the phase objects. The size for the real-space object is 75 nm (vertical) × 172 nm (horizontal). (**C-D**) The result of averaged individual reconstructions. Testing the consistency of the phase retrieval algorithm by averaging over multiple runs of the algorithm initiated by random starting conditions (*2–6*) : the algorithm is successful when the diffraction pattern of the averaged object agrees with the measured diffraction pattern. Unfortunately, the relative translations in individual reconstructions preclude us from averaging efficiently. In order to find the set of reconstructions with less relative translations, we cross-correlated the individual reconstructions and then average the set of reconstructions with highest mutual correlation. (~100 out of 2000 reconstructions) (**C**) shows the displacement field (DF), crystal-plane inclination (CI) and normal strain (NS) of the averaged object. (Top to bottom order) All three images show a periodic layered structure that agrees with the PTO/STO superlattice. (**D**) The corresponding diffraction pattern calculated from the averaged real-space phase object. The average intensity successfully reproduces the main features of the measured diffraction data, such as the satellite peaks and the Laue fringes (Laue fringes) in between.

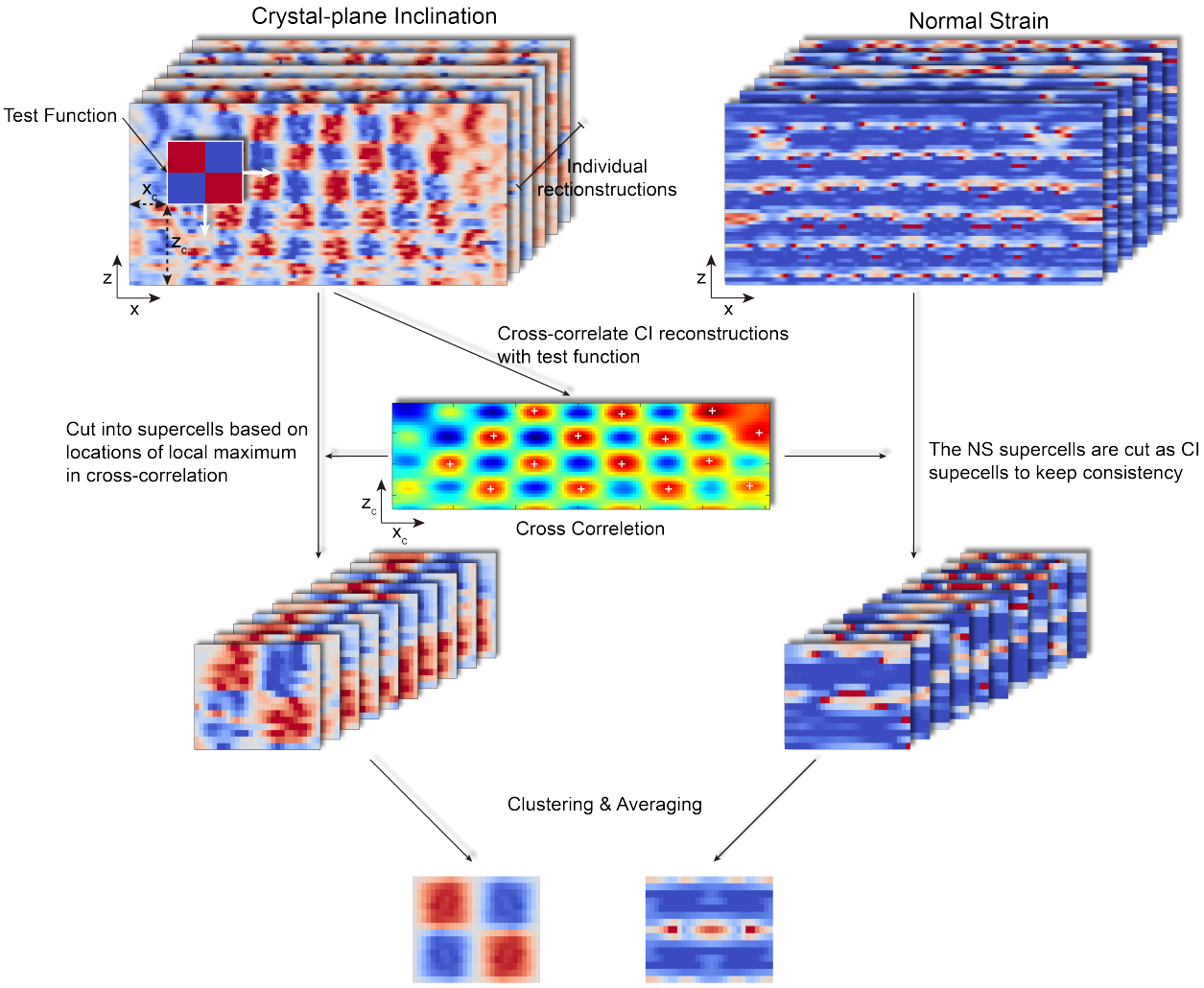

Fig. S2. Flow chart of pattern recognition from a set of individual phase retrieval reconstructions with k-means clustering. First, a sinusoidal test function is built with a size determined by mesoscale periodicity length. Then the locations of the supercells are determined by cross correlating the test function with the individual reconstructions. Finally, the separated supercells of the CI are clustered by k-means clustering and then apply the same clusters to average both NS and CI supercells.

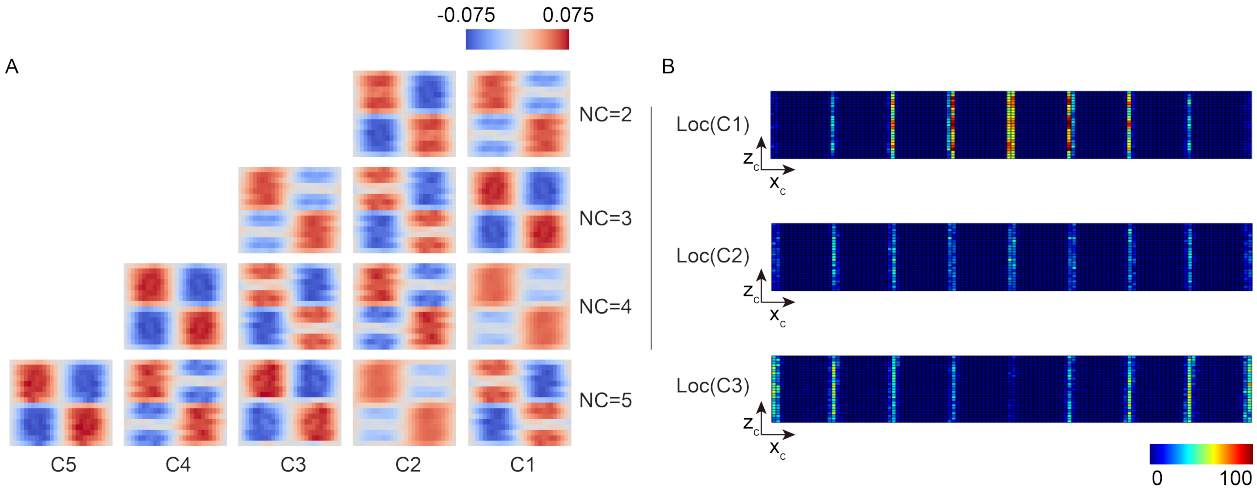

Fig. S3. Clustering results of $(PbTiO_3)_{16}/(SrTiO_3)_{16}$ data. Supercells with distinct features are grouped into different clusters by k-means clustering. The characteristic features of one cluster are shown by averaging all the supercells belonging to that cluster. (**A**) Average supercells for each cluster (C1, C2, …) from k-means clustering for increasing numbers of clusters (NC). For more than three clusters, increasing the number of clusters does not reveal additional distinct features beyond those observed with NC=3. For example, with NC=4 both C1 and C2 resemble the C3 of NC=3, and the same situation can also be observed with NC=5. (**B**) 2D histograms show the spatial distribution of the supercells assigned to each cluster for NC=3. Each reconstruction, with dimensions set by the real space support, is segmented into supercells then clustered and averaged as described in Fig. S2. These histograms show the count of supercells assigned to the cluster at each position within the support, over the full ensemble of reconstructions. Cluster C1 has the largest population and the distribution of C1 supercells is concentrated in the center of the reconstructed object where the periodic patches are mostly observed, which is the significant structural motif that composes the mesoscale periodicity. Meanwhile, the averaged patterns of C2 and C3 resemble C1 with the addition of horizontal bisection of diagonal pairs of blocks. Because C2 and C3 have smaller populations compared to C1 and are prone to appear at the reconstruction edges, the reliability of the bisection feature is questionable. Notably, in all the three histograms, the horizontal positions of the supercells are well defined and evenly spaced, while a greater position uncertainty is present in the vertical direction, which reemphasizes the necessity of averaging over supercells instead of the entire reconstructed object.

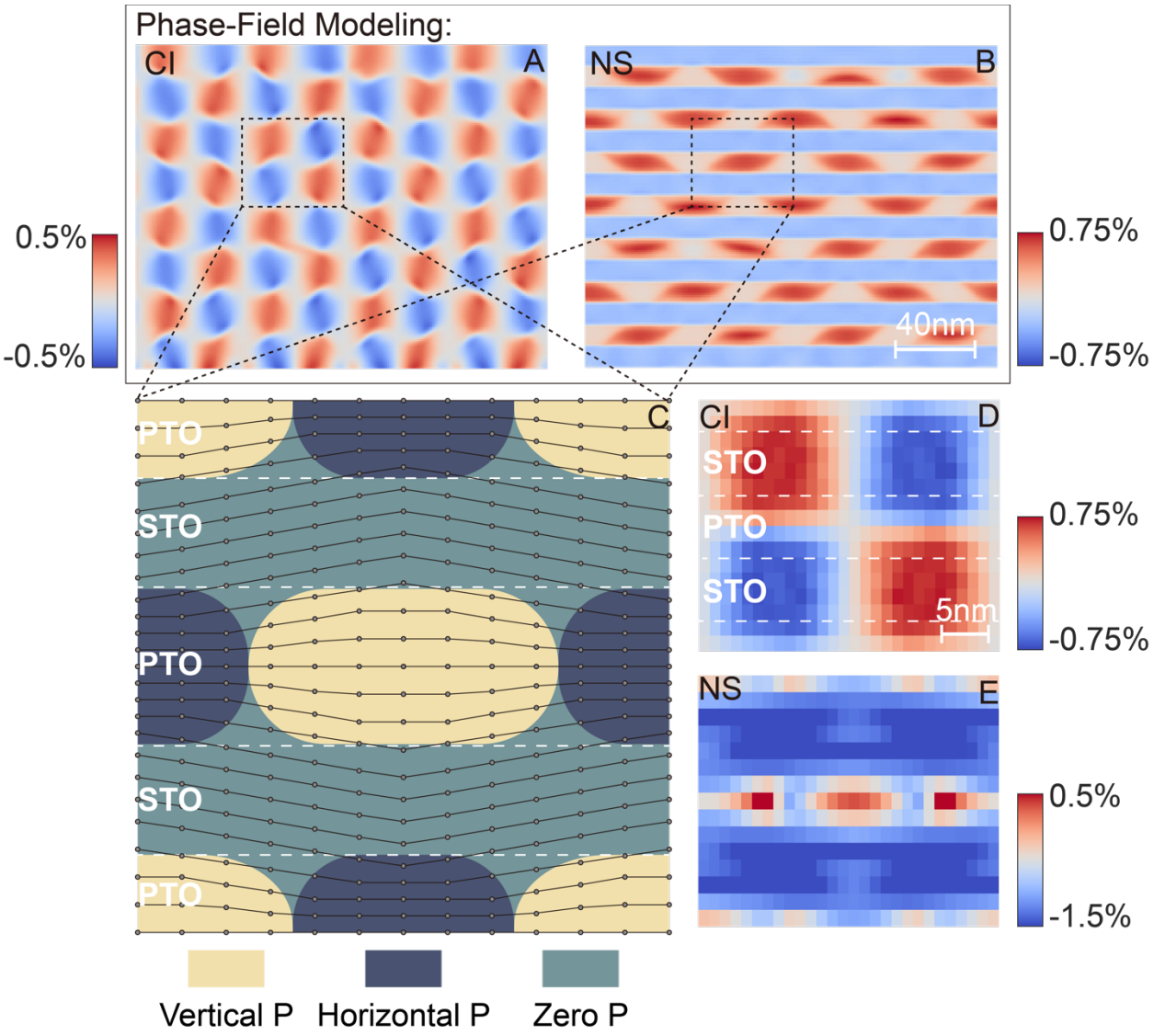

Fig. S4. Comparison of X-ray imaging results to Phase-field modeling Crystal-plane inclination map (**A**) and normal strain map (**B**) calculated from phase-field modeling result. Both maps show 2D periodicity. The corresponding supercells are indicated by dashed boxes. (**C**) Schematic of the polarization and lattice in the supercell. There are three different local polarization statuses: regions with zero polarization in STO layers, regions with dominantly vertical (along z||$[110]_{DSO}$) polarization and regions with dominantly horizontal (along x||$[\bar{1}10]_{DSO}$) polarization in PTO layers. As the direction of polarization is correlated with the distortion of the PTO unit cells, the local vertical lattice spacing can be inferred as the dots and lines shown in the schematic. The region with horizontal polarization has smaller vertical lattice spacing than the region with vertical polarization. And because of the local 'shrink' and 'expand' of the PTO layer, inclination will occur in the adjacent STO layer lattice accordingly. The crystal-plane inclination (CI) (**D**) and normal strain (NS) supercells (**E**) of our X-ray imaging agree well with the results from the phase field modeling. Both show a 2D checkerboard pattern in the CI and a layered pattern in NS. Moreover, the CI supercells from the phase field modeling also show a slightly stronger inclination around the horizontal interface of the opposite blocks, appearing a bisectional feature similar to what we observed in one of the clusters of the CI supercells (Fig. S3A).

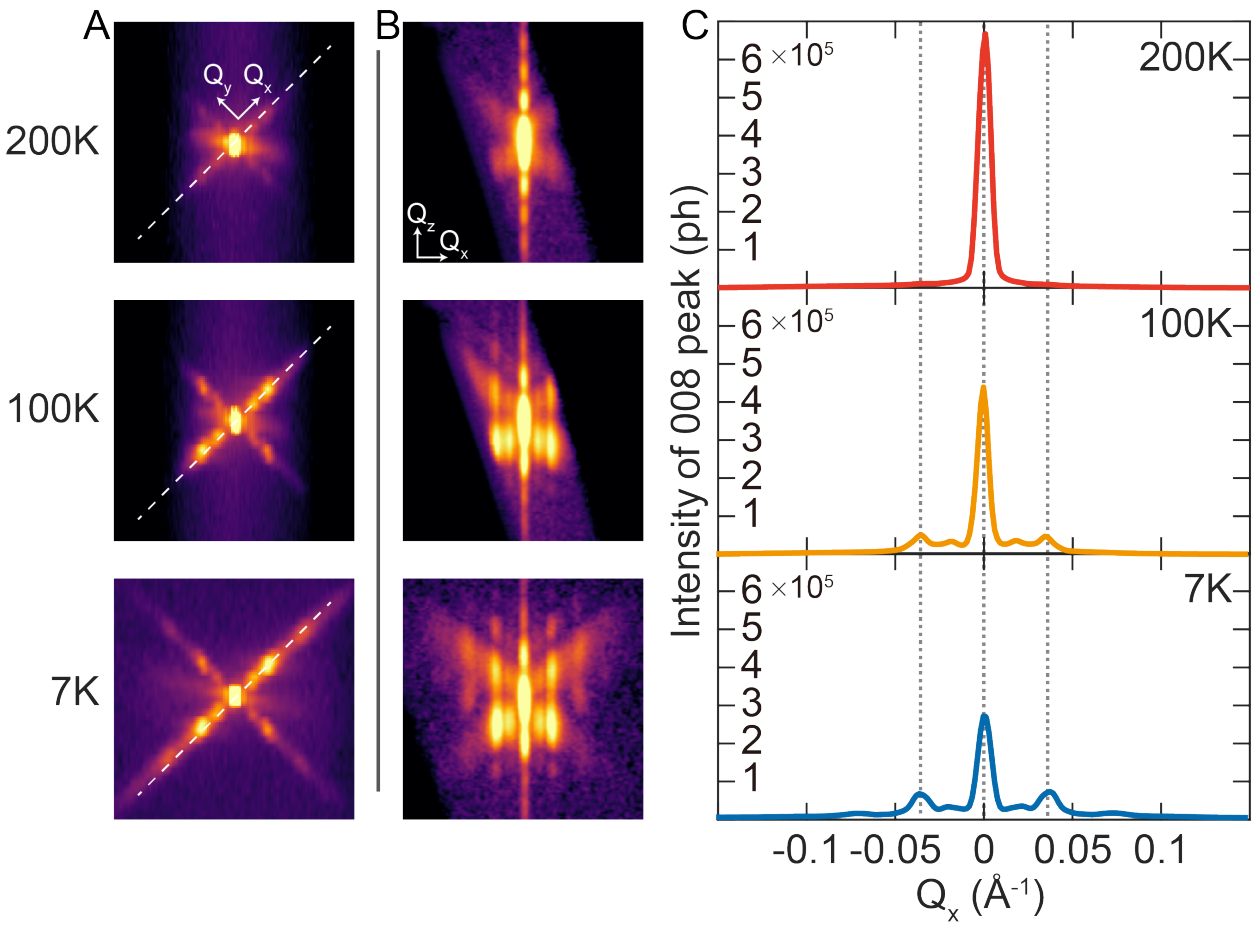

Fig. S5. Diffraction patterns under various temperatures. The reciprocal space maps (RSMs) around Ca_2RuO_4 008 Bragg peak measured with area detector using θ-scan, under 200 K, 100 K and 7 K. (**A**) Projection of the RSMs along Q_z. (**B**) The corresponding 2D slices and (**C**) line profiles along the diagonal white dashed lines in (**A**). With the decrease of temperature, the satellite peaks emerge gradually. And from the line profiles of the dashed lines as well as the projections, the spacing between the satellite peaks appear to be constant, indicating the period of the short-range order doesn't change as a function of temperature. The spacing between the satellite peaks is 0.36 nm^{-1}, corresponding to a period length of ~17.5 nm. (The θ-scans under 200 K and 100 K are measured with a smaller θ range than the 7 K and only the central part of the entire peak is recorded).

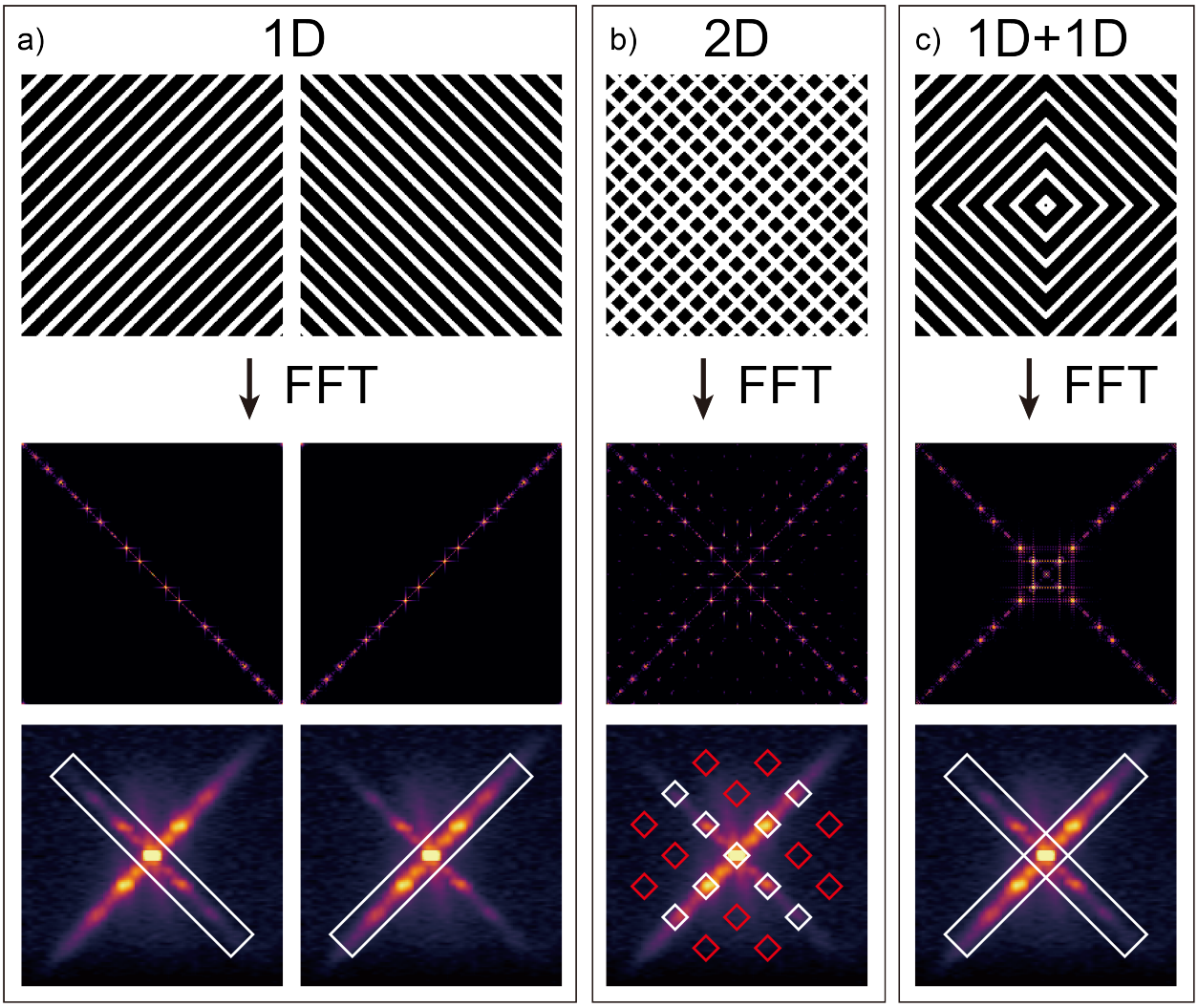

Fig. S6. Indication of spatially separated 1D periodic domains in Ca_2RuO_4 thin film (**A**) A structure with 1D periodicity will lead to a 1D periodic pattern with the same periodicity orientation after Fourier Transform (FT). (**B**) A tweed structure will lead to a 2D periodic pattern after FT. In the measured diffraction pattern of Ca_2RuO_4 film, satellite peaks only emerge on the diagonals (white boxes). And no peaks were observed at the off-diagonal positions (red boxes), which are expected from a 2D periodic tweed structure. (**C**) A spatially separated 1D periodic structure with orthogonal orientation will lead to a cross shaped diffraction pattern as observed in the diffraction pattern of Ca_2RuO_4 film. Moreover, an evident intensity difference can be observed between the two diagonals: The integral intensity of the diagonal along top-right to bot-left is approximately three times that of the other diagonal. Therefore, it seems that each diagonal streak represents spatially separated domains with 1D periodicity oriented along one of the orthogonal directions. And the relative intensity difference of the two streaks comes from the volume disparity of the two types of domains.

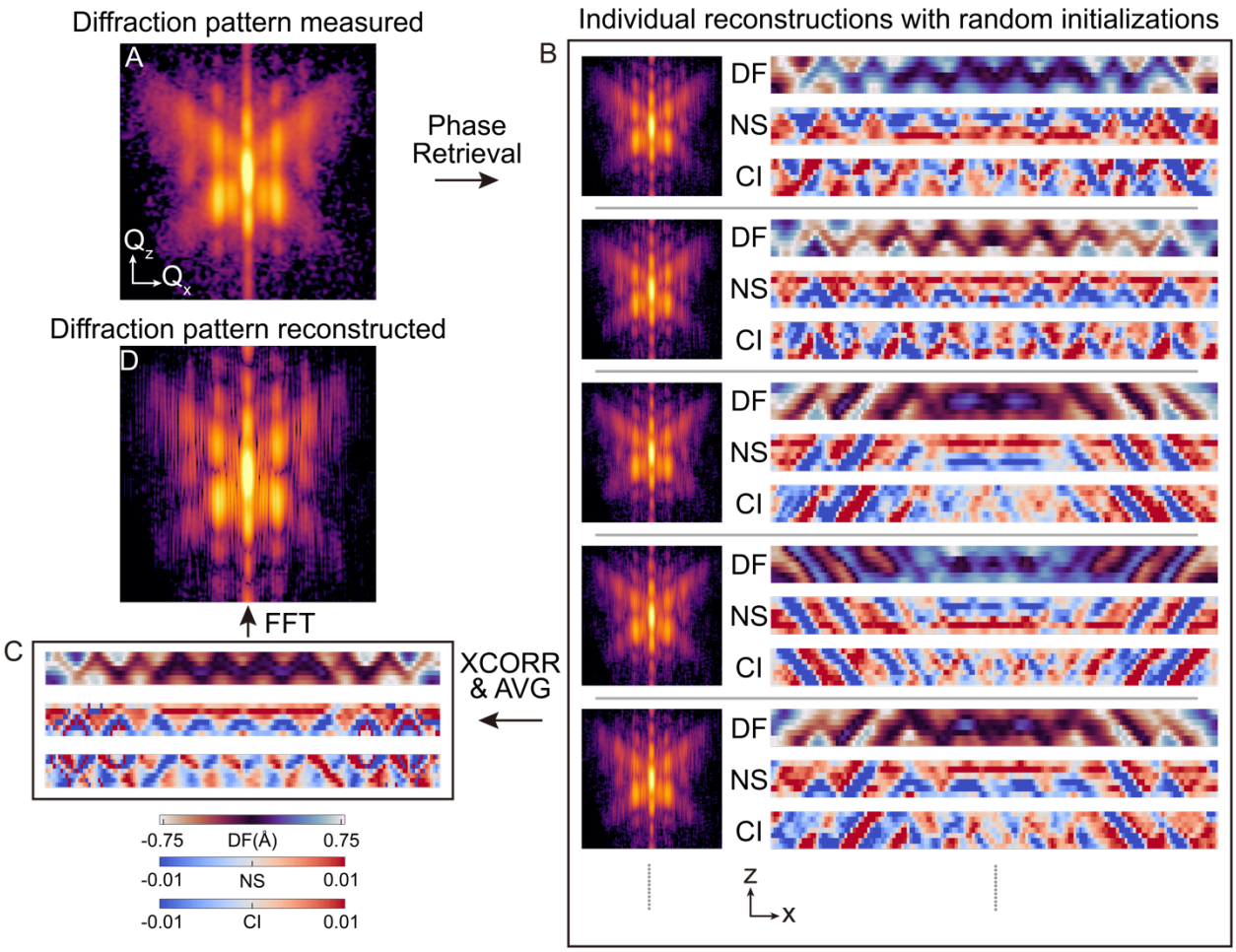

Fig. S7. Phase retrieval and individual reconstructions of Ca_2RuO_4. (**A**)Reciprocal space map (RSM) measured around Ca_2RuO_4 008 Bragg peak (**B**) The diffraction pattern and the corresponding real-space object of individual reconstructions found through iterative phase retravel algorithms with different randomized initialization. As shown, the reconstructed patterns share identical features as the measured peak and all the corresponding real-space phase objects show some level of short-range order. Meanwhile, the pattern of the corresponding real-space phase objects may vary significantly. Some show zigzag patterns, and some appear to contain diagonal stripes. Worth noticing, within the reconstructions show diagonal stripes, the numbers of stripes with two different orientations always match so that the reflection symmetry observed in the measured diffraction pattern can be retained. The size of the real-space phase object is 14 nm (vertical) *170 nm (horizontal). (**C**) The result of averaged individual reconstructions with highest mutual correlation (calculated with the same method as Fig. S1C). (**D**) The corresponding diffraction pattern calculated from the averaged real-space phase object.

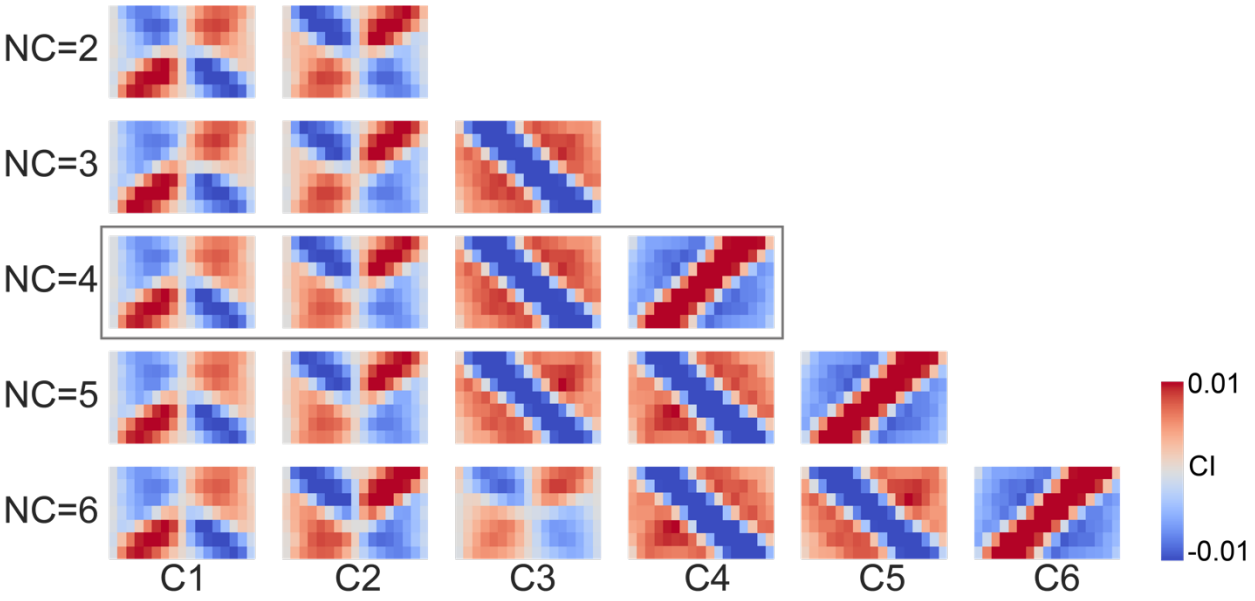

Fig. S8. Clustering results of Ca_2RuO_4 data. Averages of crystal-plane inclination (CI) supercells after k-means clustering with different number of clusters (NC). Compared to the method shown in S2, 1D instead of 2D cross-correlation is used since the periodicity only exists in one direction in Ca_2RuO_4 film. As shown, k-means clustering with four clusters results in four distinct structural motifs, while further clustering with more clusters will result in redundancy. For example, when NC=5, C3 and C4 share a similar diagonal feature; when NC=6, two pairs C2/C3, C4/C5 both show a similar feature. NC=4 is used to determine the characteristic structural motifs to avoid unnecessary excessive clustering. For NC=4, the population ratio of $C1:C2:C3:C4 \approx 2:2:1:1$. Because the C1 and C2 supercells are the majority in the reconstructions, the appearance of the zig-zag pattern in the average result (see Fig. S7) is statistically plausible as C1 and C2 get a better mutual correlation.

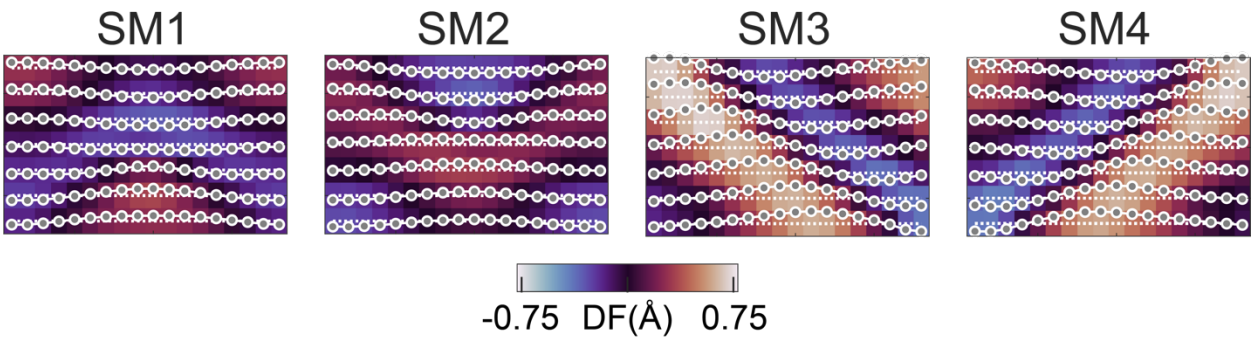

Fig. S9. Displacement field of characteristic structural motifs. According to the displacement field (DF) $u_z(x, z)$ of the structural motifs shown in Figure 4 of the main text, the linked grey dots are plotted (with an exaggerated scale for a clear view) to show the distorted lattice from the perfect unstrained lattice indicated by the underlying dashed lines. SM1 and SM2 show a reflection symmetry with respect to their central vertical line, while SM3 and SM4 show no such reflection symmetry within themselves. Instead, the SM3 and SM4 are mirror reflections of each other.

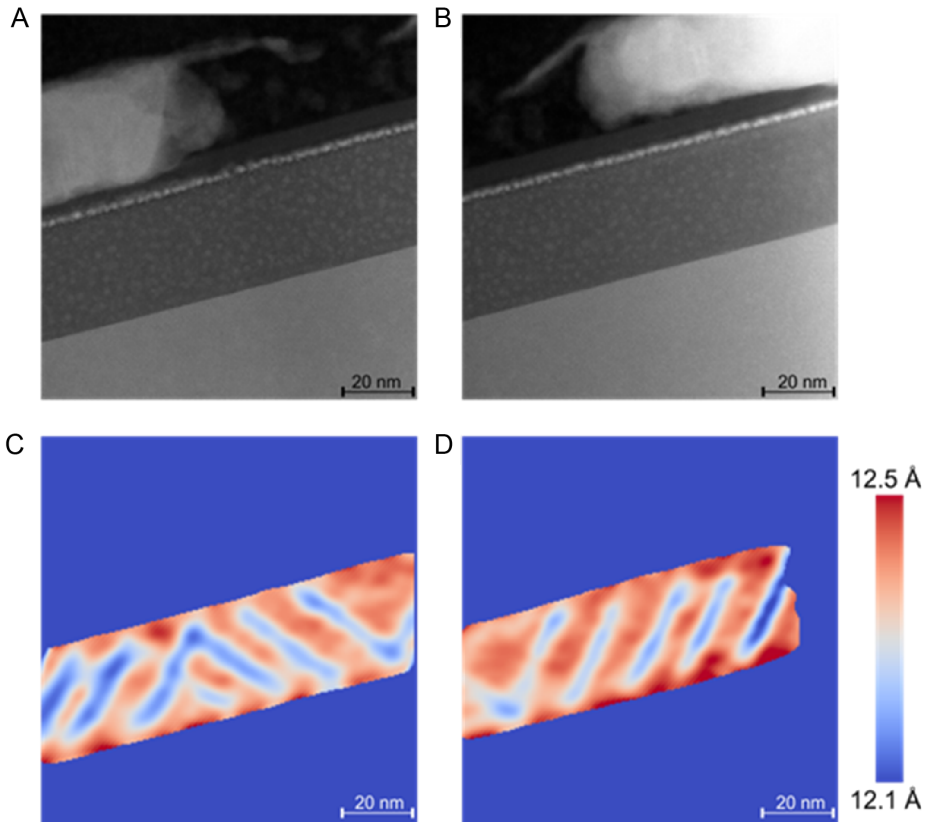

Fig. S10. Cryogenic Scanning Transmission Electron Microscopy (cryo-STEM) results. (**A,B**) Unprocessed HAADF-STEM images of the Ca_2RuO_4 film cross-section (**C,D**) Corresponding [001] interplanar spacing maps (see methods).

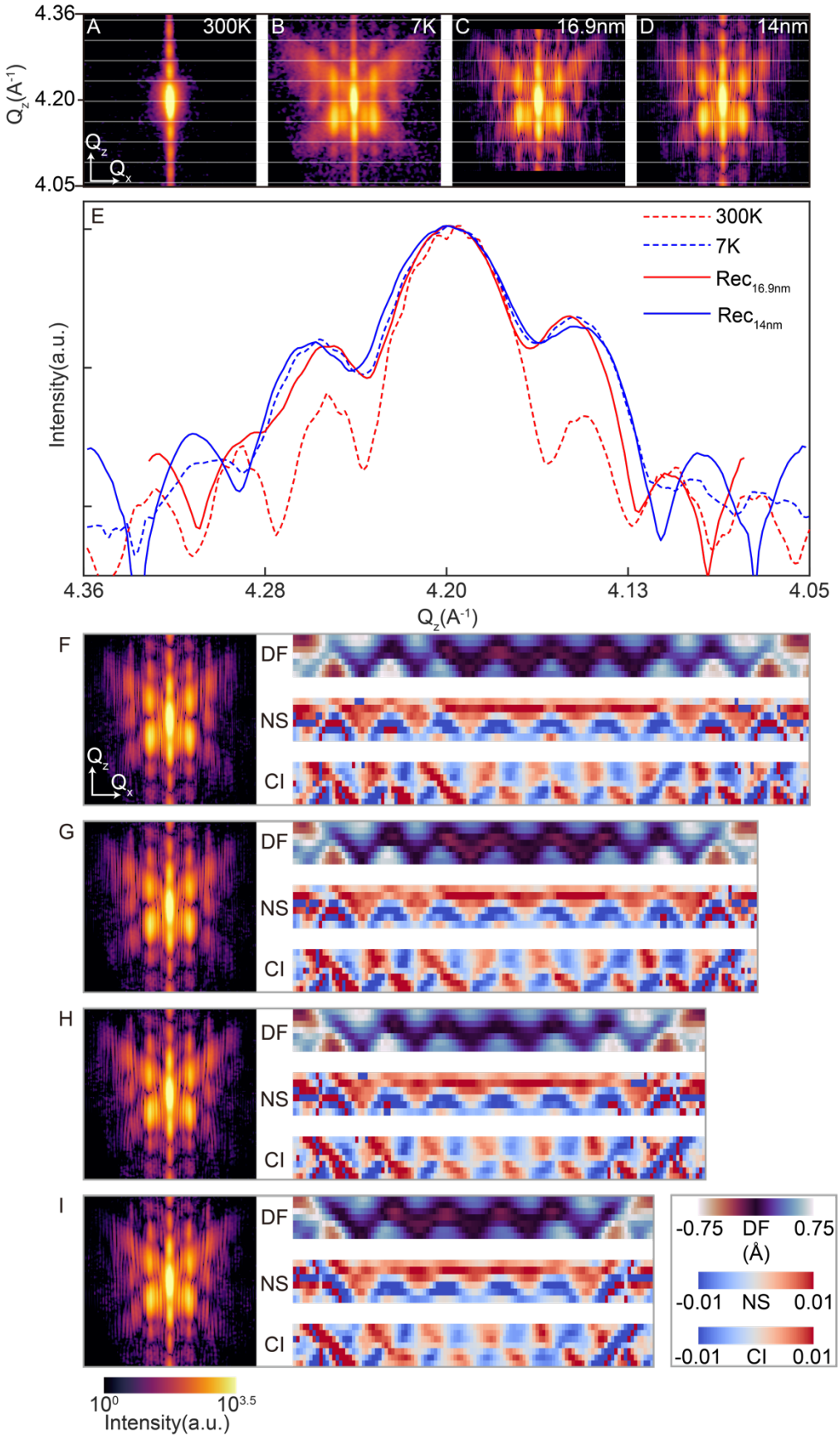
A
300K
B
7K
C
16.9nm
D
14nm
4.36
4.20
4.05
Q_z(A^-1)
Q_z
Q_x
E
300K
7K
Rec_16.9nm
Rec_14nm
Intensity(a.u.)
4.36
4.28
4.20
4.13
4.05
Q_z(A^-1)
F
G
H
I
DF
NS
CI
-0.75 DF 0.75
(Å)
-0.01 NS 0.01
-0.01 CI 0.01
10^0
10^3.5
Intensity(a.u.)

Fig. S11. Reconstruction with various support sizes (**A,B**) Measured X-ray diffraction pattern in the plane of $Q_z[001]_{LAO}$-Q_x $[110]_{LAO}$ under (**A**) 300 K and (**B**) 7 K, respectively. A difference of the Laue fringes can be noticed by comparing the two patterns (white grid is set according to the Laue fringes minimum positions at 300 K). The 300 K fringes indicate a film thickness of 17 nm, while the 7 K fringes indicate a thickness of 14 nm. The cause of the disparity of the Laue fringes under different temperatures is unclear. One plausible explanation is the illuminated region upon the thin film drifted during the dramatic change of temperatures because of the thermal expansion of the sample holder. And, as observed in the STEM, a thickness change of ~3 nm on CRO/LAO film is possible. (**C,D**) The real-space pixel size in the phase retrieval algorithm is inversely related to the reciprocal space range. By tuning the input reciprocal space image size, we performed reconstructions with various support thicknesses. The corresponding diffraction patterns reconstructed with support thickness of (**C**) 17 nm and (**D**)14 nm. (**E**) The comparison of the Laue fringes of measured and reconstructed patterns. There is an obvious difference between the two fringes measured at different temperatures especially in the off-center regions. The fringe of the 17 nm reconstruction agrees with the measured 300K fringe, and the 14 nm reconstruction fringe agrees with the measured 7K fringe. Therefore, it's demonstrated that the support thickness is directly related to the Laue fringes of the reconstructed pattern and a support thickness of 14 nm is selected to reconstruct the data measured at 7K. Compared to the support thickness, the horizontal size of the support has less effect on the reconstruction. (**F-I**) Reconstructions with thickness of 14nm and various horizontal support size of 169.5nm, 150.5nm, 133.7nm, 116.8nm. All the reconstructed diffraction patterns well retained the features of the measured data and resemble each other. And the width of the fine vertical lines within the reconstructed pattern is inversely related to the support horizontal size, as the a 'Laue fringes' analogue in the horizontal direction. Although the reconstructions are with different support sizes, similar repeating patterns are observed in all the reconstructed real-space object with different number of periods.

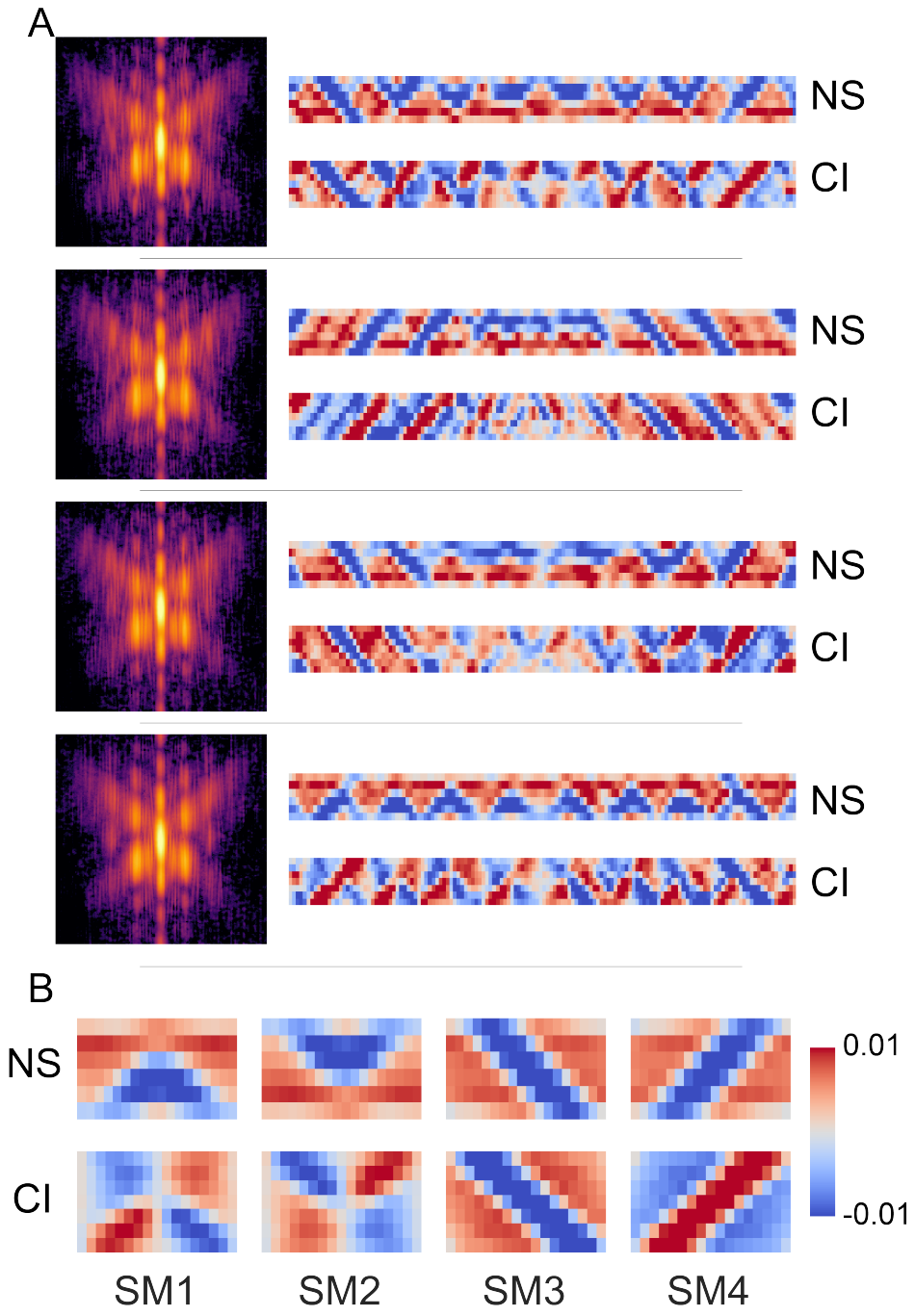

Fig. S12. Uniqueness of the structural motifs recovered. To show the uniqueness of the results, we retrieved structural motifs using a different ensemble of images than the ensemble used in Fig.4 and Fig.S8. In this new set of real space images, we increased the number of images from 2000 to 3000 and reduced the horizontal support size from 170 nm to 150 nm. (**A**) A few examples of the reconstructed diffraction patterns and the corresponding real-space images in the new ensemble. (**B**) The structural motifs recovered from the new ensemble of images, which are consistent with the results shown in the main text (see Figs. 4C and 4D). This observation suggests the motifs recovered from our approach are unique given the number of images in the ensemble is nontrivially large to represent all the possible short-range-ordered arrangement of the structural motifs. The uniqueness is not subjected to the horizontal size of the support applied.

Sample Code for 2D Phase Retrieval:

The code required for generating results shown in Figure 1 is freely available here: https://github.com/ZimingS/Periodic-Textures-Imaging.

Define support and initialize input

```
%data is a 2D matrix of diffraction intensity, with the center of the
%bragg peak aligned to the center of the matrix
srhor=80; %Support horizontal size
srver=4;  % Support vertical size
Simnum=1;%number of random starts/simulations;
Collector=zeros([size(data),Simnum]);%initialize collector for individual reconstruction results
support=zeros(size(data));
[sx,sy]=meshgrid(-size(data,2)/2:size(data,2)/2-1,-size(data,1)/2:size(data,1)/2-1);
support((abs(sx)<srhor)&(abs(sy)<srver))=1;%real-space constraint
G0=sqrt(data);%Calculate Amplitude from Diffraction Intensity(data)
G0=ifftshift(G0);
support=ifftshift(support);
```

Iterative Phase Retrieval

```
for nn=1:Simnum
    rng shuffle
    gk=exp(1j*2*pi*rand(size(data)));% random start
    for n=1:1999 %number of iteration in one reconstruction with random start
        G0c=G0;
        if mod(n,100)<60
            gk=OOPCSYM(gk,G0c,support,0.6);
        elseif mod(n,100)<80
            gk=OOPC(gk,G0c,support,0.8);
        else
            gk=OOPC(gk,G0c,support,0.98);
        end
    end
    clear Gk Gkp
    Collector(:,:,nn)=gk;
end
support=fftshift(support);
G0=fftshift(G0);
```

Custom Output-Output algorithm

```
function gkk=OOPC(gk,G0,support,beta)
Gk=ifft2(gk);
Gkp=G0.*exp(1j*angle(Gk));%Fourier space constrain
gkk=fft2(Gkp);
gkk=exp(1j*angle(gkk));
gkk=support.*gkk+(1-support).*(gkk-beta*gkk);%output-output
end
```

Custom Output-Output algorithm with real-space SYM constraint

```
function gkk=OOPCSYM(gk,G0,support,beta)
Gk=ifft2(gk);
Gkp=G0.*exp(1j*angle(Gk));%fourier space constrain
gkk=fft2(Gkp);
gkk=exp(1j*angle(gkk));
gkk=SYM(gkk);%real space symmetry constraint
gkk=support.*gkk+(1-support).*(gkk-beta*gkk);%output-output
end
```

Real Space Symmetry Constraint

```
function gkk=SYM(gkp)
gkk=exp(1j*(angle(gkp)+fliplr(angle(gkp)))/2);
end
```

SI References:

1. Stoica, V. A., Laanait, N., Dai, C., Hong, Z., Yuan, Y., Zhang, Z., Lei, S., McCarter, M. R., Yadav, A., Damodaran, A. R., Das, S., Stone, G. A., Karapetrova, J., Walko, D. A., Zhang, X., Martin, L. W., Ramesh, R., Chen, L. Q., Wen, H., *et al.* Optical creation of a supercrystal with three-dimensional nanoscale periodicity. *Nat Mater* **18**, 377–383 (2019).

2. Chapman, H. N. & Nugent, K. A. Coherent lensless X-ray imaging. *Nat Photonics* **4**, 833–839 (2010).

3. Vartanyants, I. A. & Robinson, I. K. Partial coherence effects on the imaging of small crystals using coherent x-ray diffraction. *Journal of Physics Condensed Matter* **13**, 10593–10611 (2001).

4. Fienup, J. R. Phase retrieval algorithms: a comparison. *Appl Opt* **21**, 2758 (1982).

5. Robinson, I. & Harder, R. Coherent X-ray diffraction imaging of strain at the nanoscale. *Nat Mater* **8**, 291–298 (2009).

6. Singer, A., Boucheron, L., Dietze, S. H., Jensen, K. E., Vine, D., McNulty, I., Dufresne, E. R., Prum, R. O., Mochrie, S. G. J. & Shpyrko, O. G. Domain morphology, boundaries, and topological defects in biophotonic gyroid nanostructures of butterfly wing scales. *Sci Adv* **2**, (2016).